REVIEW

The Concept of Cutting Lines in Carbon Nanotube Science

Ge. G. Samsonidze,[a] R. Saito,[d] A. Jorio,[b, e] M. A. Pimenta,[e] A. G. Souza Filho,[b, f] A. Grüneis,[d] G. Dresselhaus,[c] and M. S. Dresselhaus[a, b, *]

[a] *Department of Electrical Engineering and Computer Science, Massachusetts Institute of Technology, Cambridge, Massachusetts 02139-4307, USA*
[b] *Department of Physics, Massachusetts Institute of Technology, Cambridge, Massachusetts 02139-4307, USA*
[c] *Francis Bitter Magnet Laboratory, Massachusetts Institute of Technology, Cambridge, Massachusetts 02139-4307, USA*
[d] *Department of Physics, Tohoku University and CREST JST, Aoba, Sendai 980-8578, Japan*
[e] *Departamento de Física, Universidade Federal de Minas Gerais, Belo Horizonte, MG 30123-970, Brazil*
[f] *Departamento de Física, Universidade Federal do Ceará, Fortaleza, CE 60455-760, Brazil*

A review is presented of one-dimensional cutting lines that are utilized to obtain the physical properties of carbon nanotubes from the corresponding properties of graphite by the zone-folding scheme. Quantization effects in general low-dimensional systems are briefly discussed, followed by a more detailed consideration of one-dimensional single-wall carbon nanotubes. The geometrical structure of the nanotube is described, from which quantum confined states are constructed. These allowed states in the momentum space of graphite are known as cutting lines. Different representations of the cutting lines in momentum space are introduced. Electronic and phonon dispersion relations for nanotubes are derived by using cutting lines and the zone-folding scheme. The relation between cutting lines and singularities in the electronic density of states is considered. The selection rules for carbon nanotubes are shown to be directly connected with the cutting lines. Different experimental techniques are considered that confirm the validity of cutting lines and the zone-folding approach.

Keywords: Carbon Nanotubes, Cutting Lines, Zone-Folding, Selection Rules, Raman Scattering.

CONTENTS

1. INTRODUCTION

In this article we discuss the general effects of quantum confinement in low-dimensional structures such as quantum wells and quantum wires. We present the generic concept of cutting lines, which is here developed in detail for carbon nanotubes, as a prototype example of one-dimensional systems. Cutting lines are defined as zone-folded one-dimensional (1D) Brillouin zone (BZ) line segments, expressed in relation to their two-dimensional (2D) BZ counterparts. Electronic and phonon dispersion relations and other properties of carbon nanotubes are discussed in terms of these cutting lines, which provide valuable physical insights. Experimental evidence for the validity of the cutting-line approach is also reviewed.

1.1. Scope of This Review

Carbon nanotubes play a fundamental role in the rapidly developing field of nanoscience and nanotechnology because of their unique properties and high potential for applications.[1, 2] The use of carbon nanotubes in nanotechnology applications requires an understanding of their electronic band structure, vibrational spectra, and other relevant characteristics. All of these properties can be derived from the corresponding properties of the graphene layer by use of the zone-folding scheme,[2] though further

*Author to whom correspondence should be addressed.

  1533-4880/2003/03/431/028/$17.00+.25 doi:10.1166/jnn.2003.231

refinements are needed to account for the curvature of the nanotube wall.[3] Zone folding maps the reciprocal space of the graphene layer onto the reciprocal space of a carbon nanotube by constructing so-called cutting lines based on the geometrical structure of the carbon nanotube. The concept of cutting lines can easily be understood from the fundamental principles of quantum mechanics. For an elementary particle moving in free space, there are no restrictions on its momentum. However, if the same particle is placed in a quantum box, its momentum becomes quantized, that is, it can assume only a discrete set of values corresponding to an integral number of wave function oscillations between the edges of the quantum box. These discrete values of the momentum for a particle in a quantum box are similar to the cutting lines in the reciprocal space of a general low-dimensional system. Once the cutting lines for a given low-dimensional system are constructed, the zone-folding scheme can be applied to investigate its electronic band structure, its vibrational spectra, and other properties of interest. The zone-folding scheme, as developed in this article, is formulated for use primarily for carbon nanotubes, and it must be modified in detail when used for nanotubes or nanowires of other materials.

We have purposely selected carbon nanotubes to demonstrate the general use of the zone-folding scheme and of cutting lines for the characterization of low-dimensional systems in nanoscience for several reasons. Carbon nanotubes are known to be an excellent prototype one-dimensional material because of their extremely small diameters,[4] their distinct geometrical structure,[2] the absence of bulk material in their core (unless we are dealing with filled nanotubes[5]), and their special electronic band structure.

Georgii G. Samsonidze was born on August 8, 1976, in Russia and received his master's degree in physics from the St. Petersburg State Technical University, Russia, in 1999. He joined the Dresselhaus group in 2001 as a Ph.D. student in the Department of Electrical Engineering and Computer Science at MIT. He is currently working on single-carbon nanotube Raman spectroscopy.

Riichiro Saito was born on March 13, 1958, in Tokyo and received a Ph.D. degree in physics from the University of Tokyo in 1985. He was a research associate at the University of Tokyo and an associate professor at the University of Electro-Communication in Tokyo. Dr. Saito has been a professor in the Department of Physics, Tohoku University, since 2003. Dr. Saito wrote the book *Physical Properties of Carbon Nanotubes*, published by Imperial College Press in 1998. He received the Japan IBM prize in 1999.

Ado Jorio was born on June 11, 1972, in Brazil and received his Ph.D. degree in physics from the Federal University of Minas Gerais, Brazil, in 1999. While completing his Ph.D., he spent one year (1998) working with Dr. Roland Currat at the Laue-Langevin Institute, France. He worked for two years (2000 and 2001) with Professor M. S. Dresselhaus at MIT as a postdoctoral fel low. He is currently an associate professor of physics at the Federal University of Minas Gerais, Brazil.

Marcos A. Pimenta was born on April 11, 1958, in Belo Horizonte, Brazil, and received his Ph.D. degree in physics from the Université d'Orléans, France, in 1987. In 1997–1998 he spent a sabbatical year with Professor Dresselhaus at MIT. He is a full professor of physics at the Federal University of Minas Gerais and a co-director of the Institute of Nanoscience at UFMG-Brazil. He has made important contributions to the study of Raman spectroscopy of carbon nanotubes.

Antonio G. Souza Filho was born on June 12, 1975, in Brazil and received his Ph.D. degree in physics from the Federal University of Ceará, Brazil, in 2001. In 2001, he joined the Dresselhaus group at MIT as a Ph.D. visiting student, where he worked for 10 months on single-carbon nanotube Raman spectroscopy. He is currently an associate researcher at the Federal University of Ceará, working on aspects of Raman scattering in solids.

Alexander Grüneis was born on June 6, 1975, in Austria and received his master's degree in phys-ics while with the group of H. Kuzmany at the University of Vienna, Austria, in 2001. After that he went to Japan with support from a Monbukagakusho Scholarship to pursue his Ph.D. with the group of R. Saito. He is working on optical properties and the Raman effect in carbon nanotubes.

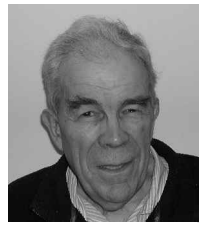

Gene Dresselhaus was born on November 7, 1929, in Ancon, Panama Canal Zone, and received his Ph.D. degree in physics from the University of California in 1955. He served one year as an instructor at the University of Chicago and four years as an assistant professor at Cornell before joining MIT Lincoln Laboratory in 1960 as a staff member. In 1977 he transferred to the MIT Francis Bitter Magnet Laboratory, where he is currently a senior scientist. His area of interest is the electronic structure of solids. He also has been broadly involved in carbon research since 1955 and carbon nanotube research since 1991 and has co-authored with M. S. Dresselhaus several books on carbon materials.

Mildred S. Dresselhaus was born on November 11, 1930 in Brooklyn, NY and received her Ph.D. degree in physics from the University of Chicago in 1958. After a two-year postdoc at Cornell University, she came to MIT Lincoln Laboratory as a staff member and has been on the MIT faculty since 1967. She is an Institute Professor of electrical engineering and physics at MIT. She has had broad interests in carbon science since 1961, and has been involved in carbon nanotube research since 1991 and carbon fiber research since 1980.

This paper, which reviews the concept of cutting lines and their use in carbon nanotube science, is organized as follows. In Section 1.2, we discuss the general concept of cutting lines and the zone-folding scheme for lower dimensionality of the material. The structure of carbon nanotubes is described in Section 2.1, followed by the development of the cutting-line theory, which is adapted to the carbon nanotube geometry. The cutting lines thus constructed are further used in the zone-folding scheme (Section 2.2) to obtain the electronic (Sections 2.3 and 2.4) and phonon (Section 2.5) dispersion relations of carbon nanotubes from the well-known dispersion relations of the 2D graphite sheet. The selection rules for optical absorption, infrared, and Raman scattering in carbon nanotubes are discussed in Section 2.6 from the point of view of cutting lines. It is shown that the cutting-line approach results in the same selection rules as the ones obtained from group theory.[6] In spite of the large number of phonon modes in carbon nanotubes, which arise from large unit cells, group theory shows that most of these are not optically active. Of those remaining, cutting lines tell us why few of the optically allowed modes give spectral features with sizable intensities. The presence of cutting lines in the reciprocal space of carbon nanotubes results in some unusual properties for carbon nanotubes when compared to graphite, as shown in Sections 2.3, 2.4, and 2.5, and these properties can be observed in various experiments, as summarized in Section 3, thus confirming the validity of the cutting-line approach and of the zone-folding scheme for carbon nanotubes. The experimental techniques discussed in Section 3 include scanning tunneling spectroscopy (Section 3.1), transport measurements (Section 3.2), and resonance Raman spectroscopy (Sections 3.1 and 3.3). Many other experimental techniques widely used in carbon nanotube science are not discussed, since they have not so far revealed any explicit information about cutting lines. Section 4 concludes with a summary.

1.2. Low-Dimensional Systems

The structural, electronic, and vibrational properties of low-dimensional systems differ substantially from the corresponding properties of their parent materials. While the parent materials are generally three-dimensional (3D) bulk crystals, the low-dimensional structures could be 2D, such as quantum wells, superlattices, and thin films; 1D, such as quantum wires and nanotubes; or zero-dimensional (0D), such as quantum dots, individual atoms, and molecules. A 2D structure has a length approximately compatible with the de Broglie wavelength of an electron in one particular direction (referred to as the nanoscale direction), while it is extended to macroscopic dimensions in the two other directions. Similarly, a 1D structure has nanoscale dimensions in two directions and it is prolonged in the third direction, while a 0D structure has nanoscale dimensions in all three directions. In fact, nanotubes have a hole in their core and, therefore, strictly speaking, cannot be considered as 1D objects, but they can be considered as quasi-1D objects. Some theories about transport in 1D systems, which apply to quantum wires, do not apply to nanotubes because of the presence of this hole.

When going from a bulk material to a low-dimensional structure, the electronic states are constrained by quantum effects in the nanoscale directions. If the low-dimensional system has the same crystal structure as the parent bulk material, the electronic states of the low-dimensional system can be considered a subset of the electronic states of the bulk material. When we move from the bulk material to the low-dimensional structure, the wave vector components in the nanoscale directions can only take on discrete values to maintain an integral number of wave function nodes, that is, these wave vector components become quantized. The number of quantized states is equal to the number of unit cells of the parent bulk material in the nanoscale directions of the low-dimensional structure. For example, if one grows a thin film from a 3D bulk crystal, the reciprocal space of the thin film can be constructed in the 3D reciprocal space of the parent bulk material by picking up only those wave vectors that lie in certain parallel equidistant planes. This is an extended representation of the 2D reciprocal space of the thin film in the 3D reciprocal space of the 3D bulk material, where each electronic energy subband in the 2D reciprocal space of the thin film corresponds to a different plane in the 3D reciprocal space of the 3D bulk material.[7]

In a similar fashion, when 1D nanotubes are rolled up from 2D sheets of 3D layered materials, such as graphite, boron nitride, or transition metal dichalcogenides, different subbands in the 1D reciprocal space of the nanotube can be extended into the 2D reciprocal space of a single sheet of the parent bulk layered material as a set of parallel equidistant lines or cutting lines, as shown in Figure 1a. The method of constructing 1D electronic energy subbands by *cutting* the 2D electronic dispersion relations with these lines is known as the "zone-folding scheme."[2] The total number of cutting lines is equal to the number of hexagons within the unit cell of the nanotube.[2] The length of each cutting line is inversely proportional to the length of a unit cell of the nanotube.[2] The separation between two adjacent cutting lines is inversely proportional to the nanotube diameter.[2] The orientation of the cutting lines in 2D reciprocal space is determined by the nanotube chiral symmetry, that is, the relative orientation of the nanotube axis with respect to the principal axes of the unrolled flat layer of the 2D parent material.[2] As an example of this general formulation, a set of cutting lines for a single-wall carbon nanotube (SWNT) is here built in the reciprocal space of the graphite sheet (see Section 2).

Although the zone-folding scheme is very useful in nanotube science, it experiences certain limitations for

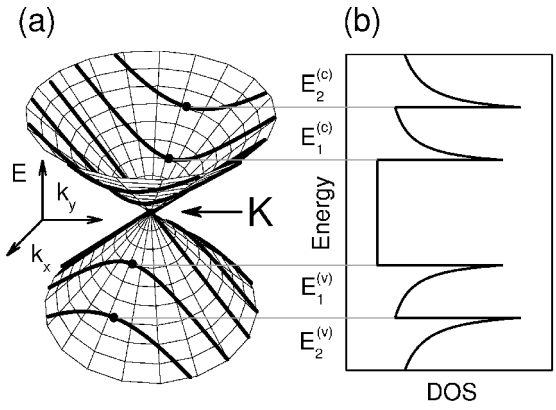

Fig. 1. (a) The energy-momentum contours for the valence and conduction bands for a 2D system, each band obeying a linear dependence of energy on wave vector and forming a degenerate point K where the two bands touch to define a zero gap semiconductor. The cutting lines of these contours denote the dispersion relation for the 1D system derived from the 2D system. Each cutting line gives rise to a different energy subband. The energy extremum E_i in each cutting line at the wave vector k_i is known as the van Hove singularity. The energies $E_i^{(v)}$and $E_i^{(c)}$ for the valence and conduction bands and the corresponding wave vectors $k_i^{(v)}$ and $k_i^{(c)}$ at the van Hove singularities are indicated on the figure by the solid dots. (b) The 1D density of states (DOS) for the conduction and valence bands in (b) corresponding to the E (k) dispersion relations for the subbands shown in (a) as thick curves. The DOS shown in (b) is for a metallic 1D system, because one of the cutting lines in (a) crosses the degenerate point (the K point in the graphite Brillouin zone). For a semiconducting 1D system, no cutting line crosses the degenerate K point, which results in a band gap opening up in the DOS between the van Hove singularities $E_1^{(v)}$ and $E_1^{(c)}$. For metallic SWNTs, the constant DOS value between $E_1^{(v)}$ and $E_1^{(c)}$ is given by $L/(\sqrt{3}\pi\gamma_0 a)$ for each cutting line crossing the K point, where L is the length of a metallic SWNT, γ_0 is the transfer integral, and α is the lattice constant for the graphene layer (see electronic dispersion for graphite around the K point in Section 2.3).

small-diameter nanotubes. In the zone-folding scheme, as described above, the effect of curvature of the nanotube wall on the electronic band structure is completely ignored, while it becomes important for nanotubes of small diameter, because of the hybridization of the electronic in-plane σ orbitals with the out-of-plane π orbitals. Furthermore, the zone-folding scheme is applicable to isolated SWNTs only, whereas, for nanotube bundles and multiwall nanotubes (or individual nanotubes dispersed on a substrate), some corrections might be required because of the weak van der Waals intertube interactions (or nanotube interactions with the substrate). In the same way as described above for electrons, the zone-folding scheme can be applied to the phonon dispersion relations for nanotubes.

Figure 1b shows the electronic density of states (DOS) related to the nanotube electronic band structure plotted in Figure 1a. Each of the cutting lines in Figure 1a (except for the one that crosses the degenerate K point) gives rise to a local maximum in the DOS in Figure 1b, known as a (one-dimensional) van Hove singularity (VHS). The four VHSs in Figure 1b are labeled $E_i^{(v)}$ and $E_i^{(c)}$ for the electronic subbands in the valence and conduction bands, correspondingly. The presence of VHSs in the DOS of 1D structures makes these structures behave quite differently from their related 3D and 2D materials, as can be seen in Figure 2. Generally, the DOS profiles for systems of different dimensionality (3D, 2D, 1D, and 0D) are very different from one another, as shown in Figure 2. The typical DOS dependence on energy $g(E)$ is given by $g \propto (E - E_0)^{[(D/2)-1]}$, where D is an integer, denoting the dimensions, and D assumes the values 1, 2, and 3, respectively, for 1D, 2D, and 3D systems.[7] Here E_0 can be considered as a critical energy in the DOS. For a 3D system, E_0 might correspond to an energy threshold for the onset of optical transitions, or to a band edge state in a semiconductor. For a 1D system, E_0 would correspond to a VHS in the DOS occurring at each subband edge, where the magnitude of the DOS becomes very large. One can see from Figure 2 that 1D systems exhibit DOS profiles that are quite similar to the case of 0D systems, with very sharp maxima at certain energies, in contrast to the DOS profiles for 2D and 3D systems, which show a more monotonic increase with energy. However, the 1D DOS is different from the 0D DOS in that the 1D DOS has a sharp threshold and a decaying tail, so that the 1D DOS does not go to zero between the sharp maxima, as the 0D DOS does (see Fig. 2). Moreover, the values of the DOS at the peak positions are generally much higher for 1D objects (nanotubes and nanowires) than for 0D objects (molecules and quantum dots), because of the much larger number of atoms in 1D objects. The extremely high values of the DOS at the VHSs allow us to observe individual 1D objects in various experiments, as discussed in Section 3.

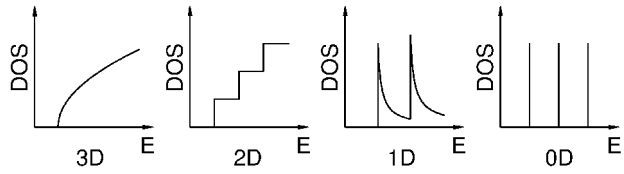

Fig. 2. Typical electronic density of states for 3D, 2D, 1D, and 0D systems.

2. THEORETICAL DESCRIPTION

We start this section by describing the geometrical structure of SWNTs. From this geometrical structure, we determine the nanotube unit cell and construct the cutting lines in the reciprocal space of the graphene layer. The translation properties of the cutting lines are then discussed, followed by the development of the zone-folding scheme for carbon nanotubes and its consequent application to the electronic and phonon dispersion relations of the graphene layer. The selection rules for the electron-photon and electron-phonon interactions in carbon nanotubes are then considered in connection with the cutting lines.

2.1. Nanotube Structure

A SWNT is constructed starting from a graphene layer (a single layer of crystalline graphite) by rolling it up into a seamless cylinder, as described elsewhere.[2] The graphene layer is oriented with respect to the coordinate system in such a way that the armchair direction lies along the x axis and the zigzag direction is along the y axis, as shown in Figure 3. The nanotube structure is uniquely determined by the chiral vector $\mathbf{C}_h$, which spans the circumference of the cylinder when the graphene layer is rolled into a tube. The chiral vector can be written in the form $\mathbf{C}_h = n\mathbf{a}_1 + m\mathbf{a}_2$, where the vectors $\mathbf{a}_1$ and $\mathbf{a}_2$ bounding the unit cell of the graphene layer with the two distinct carbon atom sites A and B are shown in Figure 3, and n and m are arbitrary integer numbers. In the shortened (n,m) form, the chiral vector is written as a pair of integers, and the same notation is widely used to characterize the geometry of each distinct (n,m) nanotube.

The nanotube can also be characterized by its diameter d_t and chiral angle θ, which determine the length $C_h = |\mathbf{C}_h| = \pi d_t$ of the chiral vector and its orientation on the graphene layer (see Fig. 3). Both d_t and θ are expressed in terms ofthe indices n and m by the relations $d_t = a\sqrt{n^2 + nm + m^2}/\pi$ and $\tan\theta = \sqrt{3}m/(2n + m)$, as one can derive from Figure 3, where $a = \sqrt{3}a_{C\text{–}C} = 0.246$ nm is the lattice constant for the graphene layer and $a_{C\text{–}C} = 0.142$ nm is the nearest-neighbor C – C distance.[2] As an example, the chiral vector $\mathbf{C}_h$ shown in Figure 3 is given by $\mathbf{C}_h = 4\mathbf{a}_1 + 2\mathbf{a}_2$, and thus the corresponding nanotube can be identified by the integer pair (4, 2). Because of the sixfold symmetry of the graphene layer, all nonequivalent nanotubes can be characterized by the (n,m) pairs of integers where $0 \le m \le n$. The nanotubes are classified as chiral ($0 < m < n$) and achiral ($m = 0$ or $m = n$), which in turn are known as zigzag ($m = 0$) and armchair ($m = n$) nanotubes. A (4, 2) nanotube is one of the smallest-diameter nanotubes ever synthesized,[4] thus requiring special calculational treatment.[8]

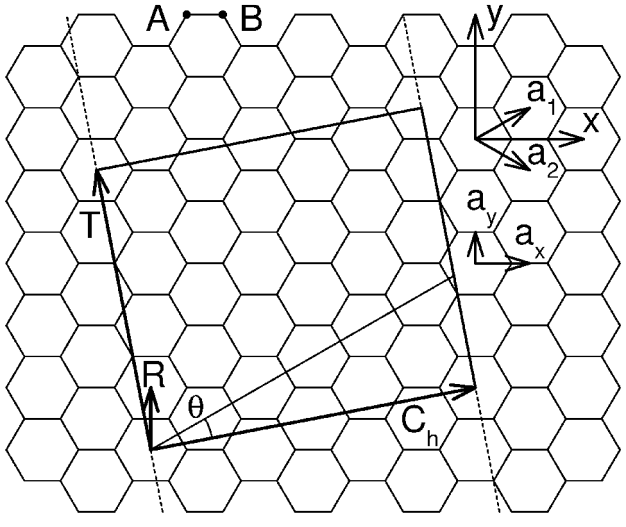

Fig. 3. An unrolled nanotube projected on the graphene layer. When the nanotube is rolled up, the chiral vector $\mathbf{C}_h$ turns into the circumference of the cylinder, and the translation vector $\mathbf{T}$ is aligned along the cylinder axis. $\mathbf{R}$ is the symmetry vector and θ is the chiral angle (see text). The unit vectors $(\mathbf{a}_1, \mathbf{a}_2)$ and $(\mathbf{a}_x, \mathbf{a}_y)$ of the graphene layer are indicated, along with the inequivalent A and B sites within the unit cell of the graphene layer.

2.1.1. Unit Cell Structure

The graphene unit vectors $\mathbf{a}_1$ and $\mathbf{a}_2$ can be written in the form $\mathbf{a}_1 = \mathbf{a}_x + \mathbf{a}_y$ and $\mathbf{a}_2 = \mathbf{a}_x - \mathbf{a}_y$, where $\mathbf{a}_x = \sqrt{3}a\hat{\mathbf{x}}/2$ and $\mathbf{a}_y = a\hat{\mathbf{y}}/2$, as shown in Figure 3. Note that the basis vectors $(\mathbf{a}_1, \mathbf{a}_2)$ are nonorthogonal, as can be easily verified by direct calculations: $\mathbf{a}_1 \cdot \mathbf{a}_1 = \mathbf{a}_2 \cdot \mathbf{a}_2 = a^2$; $\mathbf{a}_1 \cdot \mathbf{a}_2 = a^2/2$; and $\mathbf{a}_1 \times \mathbf{a}_2 = -\sqrt{3}a^2\hat{\mathbf{z}}/2$. The translation vector $\mathbf{T}$ can be obtained from the chiral vector $\mathbf{C}_h$ by counterclockwise rotation in the (x,y) plane by the angle $\pi/2$. This results in the following expression for the translation vector, $\hat{\mathbf{z}} \times \mathbf{C}_h = (m - n)\,\mathbf{a}_x/\sqrt{3} + \sqrt{3}(m + n)\mathbf{a}_y$, taking into account the nonorthogonality of the basis vectors $\mathbf{a}_1$ and $\mathbf{a}_2$. Clearly, the translation vector obtained in such a way must be further multiplied by $\sqrt{3}$ to extend over an integer number of hexagons in the graphene layer. In the nonorthogonal basis $(\mathbf{a}_1, \mathbf{a}_2)$, the translation vector then becomes $\sqrt{3}\hat{\mathbf{z}} \times \mathbf{C}_h = (2m + n)\mathbf{a}_1 - (2n + m)\mathbf{a}_2$. For a general (n,m) nanotube, the two integer numbers $(2m + n)$ and $(2n + m)$ may have a common divisor, and in this case the translation vector may be reduced to the form $\mathbf{T} = t_1\mathbf{a}_1 + t_2\mathbf{a}_2$, where $t_1 = (2m + n)/d_R$, $t_2 = -(2n + m)/d_R$, and $d_R = \gcd(2n + m, 2m + n)$, while $\gcd(\iota,\jmath)$ denotes the greatest common divisor of the two integers ι and $\jmath$. The expression for d_R can be simplified,[2] by using the fact that $\gcd(\iota,\jmath) = \gcd(\iota - \jmath, \jmath)$ if $\jmath < \iota$ (Euclid's law), resulting in $d_R = d$ if $n - m$ is not a multiple of $3d$, and $d_R = 3d$ if $n - m$ is a multiple of $3d$, where $d = \gcd(n,m)$. For zigzag nanotubes ($m = 0$), $d_R = d = n$, and $(t_1, t_2) = (1, -2)$, while for armchair nanotubes ($m = n$), $d_R = 3d = 3n$, and $(t_1, t_2) = (1, -1)$. For the (4, 2) nanotube shown in Figure 3, we have $d_R = d = 2$ and $(t_1, t_2) = (4, -5)$. The unit cell of an unrolled nanotube on a graphene layer is a rectangle bounded by the vectors $\mathbf{C}_h$ and $\mathbf{T}$ (see the rectangle shown in Fig. 3 for the (4, 2) nanotube). The area of the nanotube unit cell can easily be calculated as a vector product of these two vectors, $|\mathbf{C}_h \times \mathbf{T}| = \sqrt{3}a^2(n^2 + nm + m^2)/d_R$. Dividing this product by the area of the unit cell of a graphene layer $|\mathbf{a}_1 \times \mathbf{a}_2| = \sqrt{3}a^2/2$, one can get the number of hexagons in the unit cell of a nanotube, $N = 2(n^2 + nm + m^2)/d_R$. For the (4, 2) nanotube we have $N = 28$, so that the unit cell of the (4, 2) nanotube (see the rectangle shown in Fig. 3) contains 28 hexagons, or $2 \times 28 = 56$ carbon atoms (see Table I).

2.1.2. Symmetry Vector

The nanotube unit cell projected on the graphene layer consists of N hexagons bounded by the vectors $\mathbf{C}_h$ and $\mathbf{T}$ as

shown in Figure 3. The N hexagons are arranged equidistantly along the nanotube circumference $\mathbf{C}_h$ forming the angles of rotation around the nanotube axis $2\pi\jmath/N$, where $\jmath$ denotes the hexagons from 1 to N. The N hexagons indexed by $\jmath$ are located at the coordinates $\jmath\mathbf{R}$ on the graphene layer, where $\mathbf{R} = p\mathbf{a}_1 + q\mathbf{a}_2$ is the symmetry vector.[2] If the vector $\jmath\mathbf{R}$ goes beyond the first unit cell, it is translated back to the first unit cell by an integral number of vectors $\mathbf{T}$. The vector $\mathbf{R}$ must be selected among the vectors pointing out to the N hexagons in the nanotube unit cell as the one with the smallest component in the direction of the chiral vector $\mathbf{C}_h$, to provide the smallest rotation angle $\chi = 2\pi/N$ around the nanotube axis between the two hexagons connected by the vector $\mathbf{R}$. This implies that we have then obtained the smallest value of the scalar product $\mathbf{R} \cdot \mathbf{C}_h$, or, equivalently, the smallest absolute value of the vector product $\mathbf{R} \times \mathbf{T}$. The latter expression is equal to $(t_1q - t_2p)$ $(\mathbf{a}_1 \times \mathbf{a}_2)$, and it takes its smallest value when the integer $t_1q - t_2p$ is equal to 1. This condition uniquely determines p and q if the symmetry vector $\mathbf{R}$ is located within the nanotube unit cell, that is, $\mathbf{R} \cdot \mathbf{T}$ is within the range from 0 to $\mathbf{T} \cdot \mathbf{T}$, or, equivalently, $|\mathbf{R} \times \mathbf{C}_h|$ is within the range from 0 to $|\mathbf{T} \times \mathbf{C}_h|$. This condition results in $mp - nq$ being within the range from 1 to N. Finally, the symmetry vector (p,q) is uniquely determined by the pair of equations

$$t_1q - t_2p = 1$$

$$1 \leq mp - nq \leq N \qquad (1)$$

For the (4, 2) nanotube, the symmetry vector $\mathbf{R} = (p, q) = (1, -1)$ is shown in Figure 3. The symmetry vector $\mathbf{R}$, consisting of a rotation around the nanotube axis by the angle $\chi = 2\pi/N$ and a translation along the nanotube axis by the vector $\tau = \mathbf{T}(\mathbf{R} \cdot \mathbf{T})/(\mathbf{T} \cdot \mathbf{T})$, reflects the basic space group symmetry operation of the nanotube.[2] Performing this operation N times, in order to gain an angle $N\chi = 2\pi$, results in $N\mathbf{R} = \mathbf{C}_h + M\mathbf{T}$, where M is an integer given by $M = mp - nq$, as can easily be demonstrated[2] by substituting the vectors $\mathbf{C}_h$, $\mathbf{T}$, and $\mathbf{R}$ derived above. Thus, the basic space group symmetry operation $\mathbf{R}$ applied N times results in a full rotation around the circumferential direction $\mathbf{C}_h$ combined with a translation by M unit cells along the axial direction of the nanotube (see Table I).

2.1.3. Reciprocal Space Vectors

The unit cell of a graphene layer is defined by the vectors $\mathbf{a}_1$ and $\mathbf{a}_2$. The graphene reciprocal lattice unit vectors $\mathbf{b}_1$ and $\mathbf{b}_2$ can be constructed from $\mathbf{a}_1$ and $\mathbf{a}_2$ by using the standard definition $\mathbf{a}_i \cdot \mathbf{b}_j = 2\pi\delta_{ij}$, where δ_{ij} is the Kronecker delta. The resulting reciprocal lattice unit vectors, $\mathbf{b}_1 = \mathbf{b}_x + \mathbf{b}_y$ and $\mathbf{b}_2 = \mathbf{b}_x - \mathbf{b}_y$, where $\mathbf{b}_x = 2\pi\hat{\mathbf{k}}_x/(\sqrt{3}a)$, $\mathbf{b}_y = 2\pi\hat{\mathbf{k}}_y/a$, and a is the lattice constant for the graphene layer, form the hexagonal reciprocal lattice, as shown in Figure 4. Note the rotation of hexagons in reciprocal space (Fig. 4) relative to those in real space (Fig. 3).

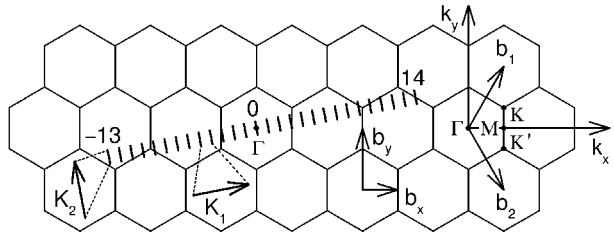

Fig. 4. Reciprocal space of the graphene layer. Parallel equidistant lines represent the cutting lines for the (4, 2) nanotube, labeled by the cutting line index μ, which assumes values from $1 - N/2 = -13$ to $N/2 = 14$. The reciprocal lattice unit vectors ($\mathbf{b}_1$, $\mathbf{b}_2$) and ($\mathbf{b}_x$, $\mathbf{b}_y$) of the graphene layer are indicated along with the (zoomed) reciprocal lattice unit vectors ($\mathbf{K}_1$, $\mathbf{K}_2$) of the nanotube.

In a similar fashion, the reciprocal space of a nanotube can be constructed.[2] The unrolled unit cell of the nanotube on a graphene layer is defined by the vectors $\mathbf{C}_h$ and $\mathbf{T}$, and therefore the reciprocal space vectors for the nanotube, $\mathbf{K}_1$ and $\mathbf{K}_2$, can be constructed by using the standard definition, $\mathbf{C}_h \cdot \mathbf{K}_1 = \mathbf{T} \cdot \mathbf{K}_2 = 2\pi$ and $\mathbf{C}_h \cdot \mathbf{K}_2 = \mathbf{T} \cdot \mathbf{K}_1 = 0$. The vector $\mathbf{K}_1$ can be written in the form $\mathbf{K}_1 \propto t_2\mathbf{b}_1 - t_1\mathbf{b}_2$ to provide its orthogonality to the vector $\mathbf{T}$, taking into account that $\mathbf{a}_i \cdot \mathbf{b}_j = 2\pi\delta_{ij}$. Similarly, $\mathbf{K}_2 \propto m\mathbf{b}_1 - n\mathbf{b}_2$ is orthogonal to $\mathbf{C}_h$. The normalization conditions $\mathbf{C}_h \cdot \mathbf{K}_1 = \mathbf{T} \cdot \mathbf{K}_2 = 2\pi$ are used to calculate the proportionality coefficients, yielding the magnitudes of the reciprocal space vectors, $|\mathbf{K}_1| = 2/d_t$ and $|\mathbf{K}_2| = 2\pi/|\mathbf{T}|$. This results in the following expressions for the reciprocal space vectors: $\mathbf{K}_1 = -(t_2\mathbf{b}_1 - t_1\mathbf{b}_2)/N$ and $\mathbf{K}_2 = (m\mathbf{b}_1 - n\mathbf{b}_2)/N$ (see Table I). Using the reciprocal space vectors $\mathbf{K}_1$ and $\mathbf{K}_2$, we can now construct the cutting lines for the nanotube. The vectors $\mathbf{K}_1$ and $\mathbf{K}_2$ are orthogonal, and $\mathbf{K}_1$ is directed along the nanotube axis, so that the cutting lines are also aligned along the tube axis.

The unrolled nanotube is prolonged in the direction of the translation vector $\mathbf{T}$ and has a nanoscale size in the direction of the chiral vector $\mathbf{C}_h$ (see Fig. 3). Since the translation vector $\mathbf{T}$ is collinear with the wave vector $\mathbf{K}_2$, and the chiral vector $\mathbf{C}_h$ corresponds to the wave vector $\mathbf{K}_1$, the unrolled reciprocal space of the nanotube (see Fig. 4) is quantized along the $\mathbf{K}_1$ direction and is continuous along the $\mathbf{K}_2$ direction. Using the expression for the vector $\mathbf{K}_1$ from the previous paragraph, one can see that $N\mathbf{K}_1 = -(t_2\mathbf{b}_1 - t_1\mathbf{b}_2)$ is a translation vector in the 2D reciprocal space of the graphene layer. This is the shortest translation vector in the given direction, since the integer numbers t_1 and t_2 do not have a common divisor by definition (see Section 2.1.1).

Consequently, the N wave vectors $\mu\mathbf{K}_1$, where μ is an integer number varying from $(1 - N/2)$ to $N/2$ (note that N is always even), form the N quantized states in the direction $\mathbf{K}_1$ of the unrolled reciprocal space of the nanotube. Each of

these N quantized states gives rise to a line segment of length $K_2 = |\mathbf{K}_2|$ along the direction $\mathbf{K}_2$ in the unrolled reciprocal space of the nanotube. These N line segments defined by the wave vectors $\mathbf{K}_1$ and $\mathbf{K}_2$ represent the cutting lines in the unrolled reciprocal space of the nanotube. The length and orientation of each cutting line in reciprocal space are given by the wave vector $\mathbf{K}_2$, and the separation between two adjacent cutting lines is given by the wave vector $\mathbf{K}_1$. In the case of our model (4, 2) nanotube, the $N = 28$ cutting lines are shown in Figure 4, numbered by the index μ varying from $1-N/2 = -13$ to $N/2 = 14$, where the middle cutting line $\mu = 0$ crosses the Γ point, the center of the first Brillouin zone of the graphene layer. In the case of an ideal, infinitely long nanotube, the wave vectors along the nanotube axis (along the $\mathbf{K}_2$ vector) would be continuous. If the nanotube length L is small enough, yet still much larger than the unit cell length $T = |\mathbf{T}|$, the wave vector along the nanotube axis also becomes quantized, $\xi(T/L)\mathbf{K}_2$, where ξ is an integer number ranging from $(2T - L)/(2T)$ to $L/(2T)$. Such quantization effects in short carbon nanotubes have been observed experimentally.[9]

2.2. Zone-Folding Scheme

The nanotube translation vector $\mathbf{T}$ is collinear with the reciprocal space vector $\mathbf{K}_2$, and therefore the first Brillouin zone of the nanotube is given by a line of length $K_2 = |\mathbf{K}_2|$. The first Brillouin zone of the nanotube is 1D because the nanotube itself is a 1D object. However, it can be expanded into the 2D reciprocal space of the graphene layer in the form of the cutting lines (see Fig. 4), in the same way as the 1D nanotube can be unrolled and placed on a 2D graphene layer (see Fig. 3). This procedure of expanding the first Brillouin zone of the nanotube into the reciprocal space of the graphene layer is known as "zone unfolding" and is opposite to the "zone-folding" scheme, as defined in Section 1.2, where the cutting lines from the reciprocal space of the graphene layer are placed together to form the first Brillouin zone of the nanotube.

The cutting lines for the (4, 2) nanotube are shown once again in Figure 5a together with the bordering rectangle drawn by dashed lines. The sides of the rectangle are given by the wave vectors $N\mathbf{K}_1$ and $\mathbf{K}_2$, so that its area can be calculated as a vector product of these two wave vectors, $N|\mathbf{K}_1 \times \mathbf{K}_2|$. Using the expressions derived in Section 2.1.3 for the wave vectors $\mathbf{K}_1$ and $\mathbf{K}_2$, we thus find the area of the bordering rectangle, $(t_1 m - t_2 n)\,|\mathbf{b}_1 \times \mathbf{b}_2|/N$. Using the relations for t_1, t_2, and N derived in Section 2.1.1, we obtain $t_1 m - t_2 n = N$, so that the area of the bordering rectangle is equal to $|\mathbf{b}_1 \times \mathbf{b}_2|$, that is, to the area of the first Brillouin zone of the graphene layer, $8\pi^2/(\sqrt{3}a^2)$. This conclusion also follows from the fact that the unit cell of the unrolled nanotube (such as the one shown in Fig. 3) consists of the N unit cells of the graphene layer, and therefore the area covered by reciprocal lattice vectors $\mathbf{K}_1$ and $\mathbf{K}_2$ for the nanotube is N times smaller than the area covered by the reciprocal lattice vectors $\mathbf{b}_1$ and $\mathbf{b}_2$ for the graphene layer.

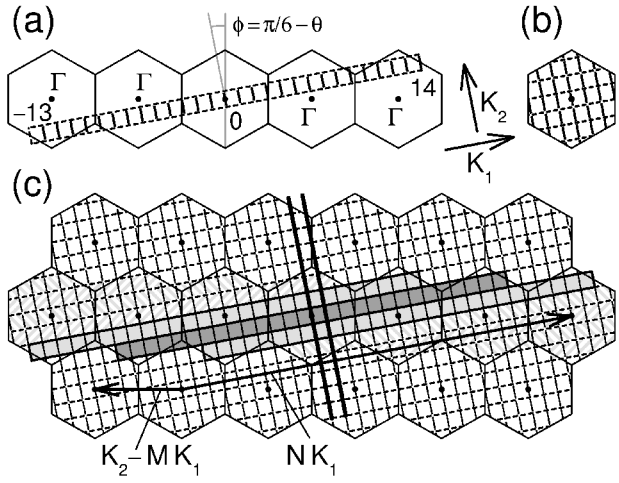

Fig. 5. Reciprocal space of the graphene layer. (a) Parallel equidistant lines give the *fully* $\mathbf{K}_1$*-extended* representation of the cutting lines for the (4, 2) nanotube. The two arrows indicate the (zoomed) reciprocal lattice unit vectors ($\mathbf{K}_1$, $\mathbf{K}_2$) of the nanotube. (b) The *fully reduced* representation of the cutting lines for the same nanotube, which is shown to fill the area of the first Brillouin zone of the graphene layer. (c) The two parallel bold line segments give the *fully* $\mathbf{K}_2$*-extended* representation of the cutting lines for the (4, 2) nanotube. Several adjacent *fully* $\mathbf{K}_1$*-extended* representations are shown in different patterns, organized in a lattice with the basis vectors $\mathbf{K}_2 - M\mathbf{K}_1$ and $N\mathbf{K}_1$. The basis vector $\mathbf{K}_2 - M\mathbf{K}_1$ indicates that the momentum change along the nanotube axis ($\mathbf{K}_2$) can be equally treated as a symmetry change in the circumferential direction ($\mathbf{K}_1$) (see the text for details).

2.2.1. Fully Reduced Representation

Because the area of the bordering rectangle is equal to the area of the first Brillouin zone of the graphene layer, the cutting lines can be shifted by the unit vectors $\mathbf{b}_1$ and $\mathbf{b}_2$ in the reciprocal space of the graphene layer to completely cover the first Brillouin zone of the graphene layer (as shown in Fig. 5b by solid lines, and dashed lines denote the ends of the cutting lines, consistent with the bordering rectangle shown in Fig. 5a). The two alternative representations of the cutting lines plotted in Figure 5a and b are called the *fully* $\mathbf{K}_1$*-extended* representation and the *fully reduced* representation, respectively, reflecting the fact that the cutting lines in Figure 5a are extended in the $\mathbf{K}_1$ direction and reduced in the $\mathbf{K}_2$ direction, and the cutting lines in Figure 5b are reduced to the first Brillouin zone of the graphene layer. By extending the cutting lines in the $\mathbf{K}_2$ direction and reducing them in the $\mathbf{K}_1$ direction, we come up with the third possible representation of the cutting lines, called the *fully* $\mathbf{K}_2$*-extended* representation (see the two parallel bold lines in Fig. 5c). Although it is easier to use the fully reduced representation of the cutting lines (see Fig. 5b) for the qualitative analysis of the nanotube

properties, either the fully $\mathbf{K}_1$-extended representation (see Fig. 5a) or the fully $\mathbf{K}_2$-extended representation (see Fig. 5c) is needed to obtain an exact band structure of the nanotube in the context of the zone-folding scheme. Below we start with the fully reduced representation, from which we construct the fully $\mathbf{K}_1$-extended representation, and finally we produce the fully $\mathbf{K}_2$-extended representation.

To build the cutting lines in the fully reduced representation for a particular (n, m) nanotube, we first determine the inclination angle ϕ of the cutting lines, namely, the angle $\phi = \pi/6 - \theta$ (where θ is the nanotube chiral angle in Fig. 3) between the cutting lines and the armchair direction $\mathbf{k}_y$ in the reciprocal space of the graphene layer.[10] Then we plot the central cutting line, originating from the Γ point (the center of the hexagon) in the first Brillouin zone of the graphene layer, until it reaches the edges of the first Brillouin zone. After that, we plot the other cutting lines parallel to the central one at the distances $|\mathbf{K}_1| = 2/d_t$ between the adjacent cutting lines (where d_t is the nanotube diameter), until we fill in the first Brillouin zone of the graphene layer. This results in the fully reduced representation of the cutting lines (see Fig. 5b). For the $\mathbf{K}_1$-extended representation, we must shorten the length of the cutting lines obtained in the fully reduced representation with a set of parallel equidistant bordering lines (see dashed lines in Fig. 5b). The bordering lines are perpendicular to the cutting lines, and the distance between the adjacent bordering lines, which is equal to the length of a cutting line in the $\mathbf{K}_1$-extended representation, is given by $|\mathbf{K}_2| = 2\pi/|\mathbf{T}|$, where $\mathbf{T}$ is the translation vector. Finally, we must shift the segments of the cutting lines by the reciprocal lattice vectors $\mathbf{b}_1$ and $\mathbf{b}_2$ to form the $\mathbf{K}_1$-extended representation of the cutting lines, such as the one shown in Figure 5a.

2.2.2. $\mathbf{K}_1$-*Extended Representation*

For a transformation between the $\mathbf{K}_1$-extended and the reduced representations of the cutting lines, it is convenient to consider translations of the whole bordering rectangle of the cutting lines in the $\mathbf{K}_1$-extended representation, such as the one shown by dashed lines in Figure 5a, in the reciprocal space of the graphene layer. As discussed above, the wave vector $N\mathbf{K}_1$ is the reciprocal lattice translation vector, so that the bordering rectangle of the cutting lines can be translated by the wave vector $N\mathbf{K}_1$ in the direction perpendicular to the cutting lines. Let us also consider a translation of the bordering rectangle along the cutting lines, that is, in the direction of the wave vector $\mathbf{K}_2$. Clearly, the translation of the bordering rectangle must be of the form $\mathbf{K}_2 - M\mathbf{K}_1$, where M is an integer number between $(1 - N/2)$ and $N/2$, that is, a translation to the next segment of the cutting line by the vector $\mathbf{K}_2$ followed by a shift of M distances between the adjacent cutting lines in the direction $\mathbf{K}_1$ perpendicular to the cutting lines. The latter shift is needed for the equivalent cutting lines in the adjacent bordering rectangles to coincide under the translation $\mathbf{K}_2$.

The number M can easily be found by considering the central cutting lines that cross the Γ points in the two adjacent bordering rectangles (see Fig. 5c). Starting from the Γ point for a given bordering rectangle (see the dark gray rectangle in Fig. 5c), the translations by the vectors $-N\mathbf{K}_1$ and $\mathbf{K}_2 - M\mathbf{K}_1$ bring us to the Γ points of the adjacent bordering rectangles. Among the Γ points of all the hexagons in the reciprocal space of the graphene layer, a translation by the vector $\mathbf{K}_2 - M\mathbf{K}_1$ selects the one that is closest to the vector $-N\mathbf{K}_1 = t_2\mathbf{b}_1 - t_1\mathbf{b}_2 \equiv (t_2, -t_1)$ (see the uppermost of the two light gray rectangles in Fig. 5c). Thus, the translation vector $\mathbf{K}_2 - M\mathbf{K}_1$ is constructed in the same way as the symmetry vector $\mathbf{R}$ in Section 2.1.2. Since the symmetry vector $\mathbf{R} = (p,q)$ is related to the nanotube translation vector $\mathbf{T} = (t_1, t_2)$ by the condition $t_1q - t_2p = 1$, the vector $-N\mathbf{K}_1 = (t_2, -t_1)$ results in the vector $\mathbf{K}_2 - M\mathbf{K}_1$ being equal to $(q, -p)$ to maintain the condition $t_1q - t_2p = 1$. Thus, the Γ points in the two adjacent bordering rectangles (the dark gray and the light gray in Fig. 5c) are separated by the vector $\mathbf{K}_2 - M\mathbf{K}_1 = q\mathbf{b}_1 - p\mathbf{b}_2$. The component of this vector in the direction along the vector $\mathbf{K}_1$ divided by the magnitude of the vector $\mathbf{K}_1$ is equal to the shift M,

$$\begin{aligned} M &= -(q\mathbf{b}_1 - p\mathbf{b}_2)\cdot\mathbf{K}_1/(\mathbf{K}_1\cdot\mathbf{K}_1) \\ &= -\tfrac{1}{2}Nd_R(qn - pm)/(n^2 + nm + m^2) \\ &= mp - nq \end{aligned} \qquad (2)$$

According to Eq. (1), the number $mp - nq$ falls in the range from 1 to N, thus involving all of the N cutting lines in the shift M. The shift $M = mp - nq$ is defined to the precision of the term N, which does not affect the relative positions of the adjacent bordering rectangles. Thus, the shift M can be defined within the range from 1 to N as given by Eq. (2), or within the range from $(1 - N/2)$ to $N/2$, similar to the cutting line index μ (see Fig. 4).

The diagram representing translations of the bordering rectangle of the cutting lines for our illustrative (4, 2) nanotube is shown in Figure 5c. The translation vectors $N\mathbf{K}_1$ and $\mathbf{K}_2 - M\mathbf{K}_1$ are shown in Figure 5c by the two arrows. The central bordering rectangle is dark gray, and the two adjacent bordering rectangles obtained from the central one by the translations $\mathbf{K}_2 - M\mathbf{K}_1$ and $-(\mathbf{K}_2 - M\mathbf{K}_1)$ are light gray. The bordering rectangles obtained by any other possible translations along the vector $\mathbf{K}_2 - M\mathbf{K}_1$ are filled with a light gray and white pattern, and the bordering rectangles obtained by the translations $N\mathbf{K}_1$ and $-N\mathbf{K}_1$, and by any other possible translations along the vector $N\mathbf{K}_1$, are white. For the (4, 2) nanotube, the shift is $M = 6$. Indeed, one can see in Figure 5c that the light gray rectangles are both shifted with respect to the dark gray rectangle in two opposite directions by six cells of the grid,

that is, by six distances between the adjacent cutting lines $K_1 = |\mathbf{K}_1|$. It is interesting to note that the shift $M = mp - nq$ given by Eq. (2) coincides with the number of translations $\mathbf{T}$ covered by the symmetry vector $N\mathbf{R}$, where $N\mathbf{R} = \mathbf{C}_h + M\mathbf{T}$ (see Section 2.1.2).

It might seem strange at first sight that the wave vector change along the nanotube axis by the vector $\mathbf{K}_2$ is equivalent to the change in circumferential direction by the vector $M\mathbf{K}_1$, but this equivalence can easily be understood by considering the symmetry vector $N\mathbf{R} = \mathbf{C}_h + M\mathbf{T}$ wrapped around the nanotube as shown in Figure 3.4 of Ref. 2. Indeed, a change of the wave vector by $\mathbf{K}_2$ results in a phase increase by 2π over the unit cell of the nanotube. This phase increase, when moving along a spiral formed by the symmetry vector $N\mathbf{R}$, sums up into $2\pi M$. The spiral of the symmetry vector $N\mathbf{R}$ spans the circumference of the nanotube. Thus, the phase increase over the circumference is given by $2\pi M$. Since the wave vector between adjacent cutting lines $\mathbf{K}_1$ provides a phase increase of 2π over the circumference, the phase increase of $2\pi M$ is equivalent to a change of the wave vector by $M\mathbf{K}_1$.

2.2.3. $\mathbf{K}_2$-*Extended Representation*

We have thus far defined the cutting lines in the fully reduced representation within the first Brillouin zone of the graphene layer, and we have extended them along the $\mathbf{K}_1$ direction to form the fully $\mathbf{K}_1$-extended representation. Similarly, we can prolong the cutting lines in the $\mathbf{K}_2$ direction,[11] and this results in another extended representation, which we call the fully $\mathbf{K}_2$-extended representation. To construct the $\mathbf{K}_2$-extended representation of the cutting lines, we start from the $\mathbf{K}_1$-extended representation as shown in Figure 5c by the dark gray rectangle. We then recall that the number of the cutting lines in the $\mathbf{K}_1$-extended representation is equal to N, and there is a shift of M cutting lines between the two equivalent cutting lines in the two adjacent $\mathbf{K}_1$-extended representations (dark gray and light gray rectangles in Fig. 5c). We thus put cutting lines along the $\mathbf{K}_2$ direction, starting from the central one, which crosses the Γ point, then picking up the Mth cutting line, then the $2M$th, and so on until we reach the $_JM$th cutting line which is beyond the $\mathbf{K}_1$-extended representation, that is, $_JM > N/2$. Then we continue with the $(_JM - N)$th cutting line, and so on until we arrange all of the N cutting lines in a single line of length $N\mathbf{K}_2$.

Clearly, we can only make this construction if M and N do not have a common divisor. If M and N have a common divisor $Q = \gcd(M,N) > 1$, we get Q lines of length $(N/Q)\mathbf{K}_2$ separated by $\mathbf{K}_1$ rather than a single line of length $N\mathbf{K}_2$. Thus, while the $\mathbf{K}_1$-extended representation always consists of the N cutting lines of length $\mathbf{K}_2$ separated by the vectors $\mathbf{K}_1$, the $\mathbf{K}_2$-extended representation consists of the Q cutting lines of length $(N/Q)\mathbf{K}_2$ separated by the vectors $\mathbf{K}_1$, where $Q = \gcd(M, N)$ may vary from 1 for some special chiral nanotubes to $N/2$ for achiral zigzag and armchair nanotubes. The $\mathbf{K}_2$-extended representation consists of a single long cutting line only for those special chiral nanotubes for which $Q = 1$, whereas for achiral zigzag and armchair nanotubes it consists of $N/2$ cutting lines of length $2\mathbf{K}_2$, thus being not much different from the $\mathbf{K}_1$-extended representation of N cutting lines of length $\mathbf{K}_2$. For our sample (4, 2) nanotube, $M = 6$, $N = 28$, $Q = 2$, and therefore the $\mathbf{K}_2$-extended representation consists of two cutting lines of length $14\mathbf{K}_2$, as shown in Figure 5c by the two parallel bold lines, and the $\mathbf{K}_1$-extended representation consists of 28 cutting lines of length $\mathbf{K}_2$, as shown in Figure 5a.

We have constructed above the translation vectors for the $\mathbf{K}_1$-extended representation of the cutting lines, $N\mathbf{K}_1$ and $\mathbf{K}_2 - M\mathbf{K}_1$. In a similar fashion, we can construct the translation vectors for the $\mathbf{K}_2$-extended representation, $(N/Q)\mathbf{K}_2$ and $Q\mathbf{K}_1 - W\mathbf{K}_2$, where W is an integer number, indicating the shift between the adjacent cutting lines in the $\mathbf{K}_2$-extended representation. By defining $Q\mathbf{K}_1 - W\mathbf{K}_2 = r_1\mathbf{b}_1 - r_2\mathbf{b}_2$, we immediately obtain $W = r_2t_2 - r_1t_1$, where the pair of integers (r_1, r_2) is uniquely determined from the two conditions $nr_1 - mr_2 = Q$ and $1 \leq t_2r_2 - t_1r_1 \leq N/Q$, similar to the pair (p,q) in Eq. (1). For the (4, 2) nanotube, $Q = 2$ and $(r_1, r_2) = (0,-1)$, so that $W = -t_2 = 5$, and the vector $Q\mathbf{K}_1 - W\mathbf{K}_2 = 2\mathbf{K}_1 - 5\mathbf{K}_2 = \mathbf{b}_2$, as can be seen from Figure 5c. Further comparison of the $\mathbf{K}_1$-extended and $\mathbf{K}_2$-extended representations of the cutting lines is continued in Sections 2.5 and 2.6. All nanotube parameters defined so far are summarized in Table I.

2.3. Electronic Dispersion

In this section we apply the zone-folding scheme to the electronic dispersion relations of the graphene layer. The properties of the nanotube electronic band structure thus obtained are then studied, including the appearance of the VHSs in the DOS (which is discussed in more detail in Section 2.4) and the classification of these properties into those that are characteristic of the two types of metallic and two types of semiconducting tubes.

With the zone-folding scheme, the electronic band structure of the nanotube can easily be obtained by superimposing the cutting lines in the $\mathbf{K}_1$-extended representation on the electronic bands of the graphene layer. Two carbon atoms A and B per unit cell of the graphene layer (see Fig. 3) have one free π-electron each, resulting in the appearance of the valence and conduction bands in the electronic band structure of the graphene layer.[2] The valence π and conduction π^* bands touch each other at the Fermi level at the K and K' points in reciprocal space (see Fig. 4), whereas the other electronic energy bands, corresponding to the sp^2-hybridized electrons involved in the covalent bonds, lie far away in energy from the Fermi level. The total number of cutting lines in the $\mathbf{K}_1$-extended

Table I. Parameters for single-wall carbon nanotubes.[a]

Symbol	Name	Formula	Value	Example (4, 2)
a	Graphene lattice constant	$a = \sqrt{3}\, a_{C-C} = 0.246$ nm	$a_{C-C} = 0.142$ nm	
$\mathbf{a}_1$, $\mathbf{a}_2$	Graphene unit vectors	$\left(\frac{\sqrt{3}}{2}, \frac{1}{2}\right)a$, $\left(\frac{\sqrt{3}}{2}, -\frac{1}{2}\right)a$	x, y coordinates	
$\mathbf{b}_1$, $\mathbf{b}_2$	Graphene reciprocal lattice unit vectors	$\left(\frac{1}{\sqrt{3}}, 1\right)\frac{2\pi}{a}$, $\left(\frac{1}{\sqrt{3}}, -1\right)\frac{2\pi}{a}$	k_x, k_y coordinates	
$\mathbf{C}_h$	Nanotube chiral vector	$\mathbf{C}_h = n\mathbf{a}_1 + m\mathbf{a}_2 \equiv (n,m)$	$0 \le m \le n$	(4, 2)
C_h	Length of $\mathbf{C}_h$	$C_h = \lvert\mathbf{C}_h\rvert = a\sqrt{n^2 + m^2 + nm}$		1.301 nm
d_t	Nanotube diameter	$d_t = C_h/\pi$		0.414 nm
θ	Nanotube chiral angle	$\tan\theta = \frac{\sqrt{3}m}{2n+m}$	$0 \le \theta \le \frac{\pi}{6}$	19.11°
		$\sin\theta = \frac{\sqrt{3}m}{2\sqrt{n^2+m^2+nm}}$, $\cos\theta = \frac{2n+m}{2\sqrt{n^2+m^2+nm}}$		
d	$\gcd(n,m)$[b]		$1 \le d \le n$	2
d_R	$\gcd(2n+m, 2m+n)$[b]	$d_R = \begin{cases} d & \text{if } (n-m) \text{ is not a multiple of } 3d \\ 3d & \text{if } (n-m) \text{ is a multiple of } 3d \end{cases}$	$1 \le d_R \le 3n$	2
N	Number of hexagons in the nanotube unit cell	$N = \frac{2(n^2+m^2+nm)}{d_R}$	Even	28
$\mathbf{T}$	Translational vector along nanotube axis	$\mathbf{T} = t_1\mathbf{a}_1 + t_2\mathbf{a}_2$	$\mathbf{T} \equiv (t_1, t_2)$	(4,−5)
t_1, t_2		$t_1 = \frac{2m+n}{d_R}$, $t_2 = -\frac{2n+m}{d_R}$	$\gcd(t_1, t_2) = 1$[b]	
T	Length of $\mathbf{T}$	$T = \lvert\mathbf{T}\rvert = \frac{\sqrt{3}C_h}{d_R}$		1.127 nm
$\mathbf{R}$	Symmetry vector of the nanotube	$\mathbf{R} = p\mathbf{a}_1 + q\mathbf{a}_2$	$\mathbf{R} \equiv (p,q)$	(1,−1)
p, q		$t_1q - t_2p = 1$, $1 \le mp - nq \le N$	$\gcd(p,q) = 1$[b]	
τ	Pitch of $\mathbf{R}$	$\tau = \frac{(mp-nq)T}{N} = \frac{MT}{N}$	$T/N \le \tau \le T$	0.242 nm
χ	Rotation angle of $\mathbf{R}$	$\chi = \frac{2\pi}{N}$	$0 < \chi \le \pi$	12.86°
M	Number of $\mathbf{T}$ in $N\mathbf{R}$	$N\mathbf{R} = \mathbf{C}_h + M\mathbf{T}$, $M = mp - nq$	$1 \le M \le N$	6
$\mathbf{K}_1$	Nanotube reciprocal lattice unit vectors	$\mathbf{K}_1 = -(t_2\mathbf{b}_1 - t_1\mathbf{b}_2)/N$	$(-t_2/N, t_1/N)$	$\left(\frac{5}{28}, \frac{1}{7}\right)$
$\mathbf{K}_2$		$\mathbf{K}_2 = (m\mathbf{b}_1 - n\mathbf{b}_2)/N$	$(m/N, -n/N)$	$\left(\frac{1}{14}, -\frac{1}{7}\right)$
		$K_1 = \lvert\mathbf{K}_1\rvert = 2/d_t$, $K_2 = \lvert\mathbf{K}_2\rvert = 2\pi/T$		
		$\mathbf{K}_1 \parallel \mathbf{C}_h$, $\mathbf{K}_2 \parallel \mathbf{T}$		
	Translational vectors for the $\mathbf{K}_1$-extended representation of the cutting lines	$N\mathbf{K}_1 = -t_2\mathbf{b}_1 + t_1\mathbf{b}_2$	$(-t_2, t_1)$	(5, 4)
		$\mathbf{K}_2 - M\mathbf{K}_1 = \frac{m+Mt_2}{N}\mathbf{b}_1 - \frac{n+Mt_1}{N}\mathbf{b}_2$	$\left(\frac{m+Mt_2}{N}, -\frac{n+Mt_1}{N}\right)$	(−1,−1)
	Translational vectors for the $\mathbf{K}_2$-extended representation of the cutting lines	$(N/Q)\mathbf{K}_2 = \frac{m}{Q}\mathbf{b}_1 - \frac{n}{Q}\mathbf{b}_2$	$\left(\frac{m}{Q}, -\frac{n}{Q}\right)$	(1,−2)
		$Q\mathbf{K}_1 - W\mathbf{K}_2 = r_1\mathbf{b}_1 + r_2\mathbf{b}_2$	(r_1, r_2)	(0,−1)
Q		$Q = \gcd(M,N)$[b]	$1 \le Q \le \frac{N}{2}$	2
W		$W = r_2t_2 - r_1t_1$	$1 \le W \le \frac{N}{Q}$	5
r_1, r_2		$nr_1 - mr_2 = Q$, $1 \le t_2r_2 - t_1r_1 \le \frac{N}{Q}$	$\gcd(r_1, r_2) = 1$[b]	

[a] In this table n, m, t_1, t_2, r_1, r_2, p, and q are integers and d, d_R, N, M, Q, and W are integer functions of these integers.
[b] $\gcd(n,m)$ denotes the greatest common divisor of the two integers n and m.

representation is equal to the number of hexagons in the nanotube unit cell, N. Therefore, by superimposing N cutting lines on the two energy-momentum contours of the valence and conduction bands in the 2D reciprocal space of the graphene layer, one will obtain $2N$ electronic energy subbands in the 1D reciprocal space of the nanotube. Since there are two atoms per unit cell in the graphite layer, the total number of atoms in the nanotube unit cell is $2N$. Therefore, the total number of electronic energy subbands in the 1D reciprocal space of the nanotube is equal to the

total number of atoms in the nanotube unit cell, in agreement with the fact that there is one free π-electron per sp^2-hybridized carbon atom. However, the total number of *distinct* electronic energy subbands is less than $2N$, since most of them are doubly degenerate. That is, the $2(N/2 - 1)$ pairs of the subbands arising from the cutting lines of the indices μ and $-\mu$, where $\mu = 1, \ldots, (N/2 - 1)$, belong to the E irreducible representations and are doubly degenerate, whereas the 4 subbands arising from the cutting lines of the indices $\mu = 0$ and $\mu = N/2$ belong to the A irreducible representations and are nondegenerate, so that the total number of the distinct electronic energy subbands is $(N + 2)$.

The energy-momentum contours for the valence and conduction bands of the graphene layer in the first Brillouin zone, calculated by using the π-band nearest-neighbor tight-binding approximation,[2] are shown in Figure 6a. The solid curves plotted in Figure 6a on the energy-momentum contours indicate the cutting lines for our sample (4, 2) nanotube in the fully reduced representation, and the solid dots stand for the ends of the cutting lines in the $\mathbf{K}_1$-extended representation. Following the zone-folding scheme, we now place the $E(k)$ for all of the cutting lines from Figure 6a in the 1D Brillouin zone of the (4, 2) nanotube, as shown in Figure 6b. The corresponding density of electronic states (DOS) for the band diagram in Figure 6b is shown in Figure 6c. One can clearly observe the presence of spikes, or VHSs, in the DOS of the (4, 2) nanotube in Figure 6c, in agreement with the general statements made in Section 1.2.

Each VHS in the DOS profile arises from a different cutting line. VHSs appear at those points of the cutting lines where the cutting lines are tangential to the electronic equi-energy contours of the graphene layer in the 2D reciprocal space. The height of the VHS is determined by the curvature of the electronic energy subband, that is, by the effective mass. For achiral (zigzag and armchair) nanotubes, each cutting line gives rise to one or two VHSs in the DOS (except for those cutting lines of zigzag metallic nanotubes that cross the K or K' points), as can easily be seen from the structure of the cutting lines for achiral nanotubes and from the band diagram of the graphene layer shown in Figure 6a. For some of the chiral nanotubes, however (when N is much larger than $n + m$, i.e., d_R is much smaller than $n + m$), the number of cutting lines in the $\mathbf{K}_1$-extended representation can be much larger than in the case of achiral nanotubes, and the length of each cutting line is much shorter. In this case, most of the cutting lines result in energy bands that are monotonically increasing or monotonically decreasing with wave vector (see, for example, the energy bands in Figure 6b around the energy of 10 eV). Many of these cutting lines have no VHSs associated with them, because the VHSs only appear at the local extrema (minima or maxima) of the 1D energy bands.

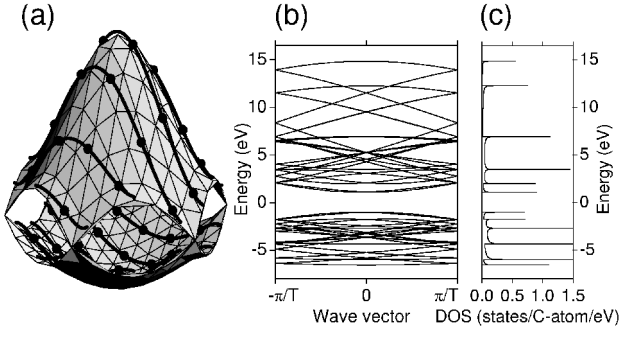

Fig. 6. (a) The conduction and valence bands of the graphene layer in the first Brillouin zone calculated according to the π-band nearest-neighbor tight-binding model.[2] Solid curves show the cutting lines for the (4, 2) nanotube in the fully reduced representation. Solid dots show the ends of the cutting lines in the fully $\mathbf{K}_1$-extended representation. (b) Band diagram for the (4, 2) nanotube obtained by zone-folding from (a). (c) Density of electronic states for the band diagram shown in (b).

To identify the VHSs in the DOS of the chiral nanotubes, it is more convenient to use the fully reduced representation of the cutting lines (see Fig. 5b) rather than the $\mathbf{K}_1$-extended representation (see Fig. 5a). Since the length of the cutting lines in the fully reduced representation is determined by the size of the first Brillouin zone of the graphene layer and is not related to the nanotube structure, each cutting line in the fully reduced representation results in one, two, or three VHSs in the DOS. Therefore, the number of the VHSs in the DOS of both chiral and achiral nanotubes is determined by the number of cutting lines in the fully reduced representation, which in turn is inversely proportional to the distance between two adjacent cutting lines $|\mathbf{K}_1| = 2/d_t$, and is not related to the number of electronic subbands in the 1D band diagram of the nanotube, $2N$. Indeed, the size of the first Brillouin zone of the graphene layer in the $\mathbf{K}_1$ direction, $(8/3)\ (\pi/a)\ \cos\theta$, divided by the distance between two adjacent cutting lines, $|\mathbf{K}_1| = 2/d_t$, yields the number of cutting lines in the fully reduced representation, $[(4\pi/3)\ (d_t/a)\ \cos\theta] + 1$, where $[x]$ indicates an integer part of x. We thus conclude that the number of VHSs in the DOS of a nanotube is proportional to the nanotube diameter d_t and only weakly depends on the nanotube chiral angle θ or on the unit cell structure of the nanotube.[12] For our illustrative (4, 2) nanotube, although all VHSs in Figure 6c correspond to different cutting lines in Figure 6a (or different subbands in Fig. 6b), not all cutting lines (or subbands) produce VHSs. The six VHSs in the valence band and in the conduction band of Figure 6c, numbered as we move away from the Fermi level $E_F = 0$, arise from the 10 cutting lines with the indices ± 9, ± 10, 14, ± 2, ± 1, and 0 (the $\pm$ sign indicates the doubly degenerate subbands), in the $\mathbf{K}_1$-extended representation (see Fig. 5a), correspondingly, whereas the other 18 cutting lines (with the indices ± 3, ± 4, ± 5, ± 6, ± 7, ± 8, ± 11, ± 12, and ± 13) do not produce VHSs in the DOS.

In contrast to most materials where the electronic energy bands near the band edge show a quadratic dependence on

wave vector, the conduction and valence bands of the graphene layer show an approximately linear dependence on wave vector near the K and K' hexagonal corners of the Brillouin zone, where they touch each other at the Fermi level.[2] Such an unusual behavior of the energy bands is related to the presence of the two inequivalent A and B atoms (see Fig. 3) in the unit cell of the graphene layer, which are related by spatial inversion symmetry. The electronic dispersion relations of the graphene layer in the vicinity of the K or K' points can be written in a linear form, $E = \pm\sqrt{3}\gamma_0 ka/2$, where the $\pm$ sign corresponds to the conduction (+) and valence (−) bands, γ_0 is the transfer integral, a is the lattice constant for the graphene layer, and k is the wave vector measured from the K or K' points.[2] According to *ab initio* calculations for the graphene layer,[13] the values for the transfer integral $\gamma_0 = 3.033$ eV and the overlap integral $s = 0.129$ (the latter is responsible for the asymmetry between the valence and conduction bands of the graphene layer) were used to calculate the electronic dispersion relations in Figure 6. From an experimental standpoint, the value of s is set to zero (no asymmetry), and the value of γ_0 is fitted to match the experimental results, yielding values between 2.5 eV and 3 eV, depending on the specific experimental measurement technique (see Section 3), thus being different from the *ab initio* value $\gamma_0 = 3.033$ eV. Furthermore, even for a small energy range of several electron volts around the Fermi level, which is the range of our greatest interest with respect to the electronic band structure, the linear approximation for the electronic dispersion relations fails because of the anisotropy of the equi-energy contours around the K and K' points. Known as the trigonal warping effect,[14] the anisotropy in the electronic dispersion relations of the graphene layer around the K and K' points results in (i) a splitting of the VHSs in the DOS of metallic nanotubes, (ii) a dependence of the VHSs on the nanotube chiral angle θ at approximately constant tube diameter d_t, and (iii) many other effects on the electronic band structure of SWNTs.[15]

Another deviation from the simple linear approximation for the electronic dispersion relations of the graphene layer arises from the σ-π hybridization of the electronic orbitals caused by the curvature of the nanotube wall.[3] Curvature opens up a band gap in the electronic dispersion relations of all metallic SWNTs other than armchair SWNTs at the Fermi level near the K and K' points, and affects the electronic band structure in many other ways. The curvature effect scales inversely with nanotube diameter, being especially important for small-diameter nanotubes, such as our sample (4, 2) nanotube. The simple π-band nearest-neighbor tight-binding approximation used in Figure 6 is not able to describe curvature effects,[16] since the description of nanotube curvature requires at least four orbitals per carbon atom, σ, π_x, π_y, and π_z. Furthermore, next nearest-neighbor interactions also affect the electronic band structure of a graphene layer, except in the vicinity of the K and K' points, as shown by comparison of the first nearest-neighbor and the third nearest-neighbor approximations with the results of *ab initio* electronic band structure calculations.[17] Thus, we conclude that Figure 6 does not reflect the real electronic band structure of a (4, 2) nanotube, being only a lowest-order approximation in the limit of small-diameter SWNTs where more detailed calculations are necessary. *Ab initio* calculations for a (4, 2) nanotube yield quite a different electronic band structure, yet they confirm its semiconducting type predicted by the zone-folding scheme.[8] In contrast, a (5, 0) nanotube, also being semiconducting within the zone-folding scheme, is in fact shown to be metallic by *ab initio* calculations.[8]

For use in interpreting experiments, the electronic band structure of a carbon nanotube is better described by the use of the Slater-Koster formalism,[18] which is based on the nanotube symmetry and introduces a number of symmetry-based parameters to achieve the accuracy needed to describe specific experiments. Instead of using *ab initio* calculations, these band parameters are fitted to experimental results. Considering only one parameter in the Slater-Koster formalism, results in the same model for the electronic dispersion relations[19] as the one obtained from the π-band nearest-neighbor tight-binding approximation, with the transfer integral γ_0 determined experimentally but without explicitly considering the overlap integral s, that is, $s = 0$. This simplest possible model therefore assumes mirror subbands for the valence and conduction bands of the graphene layer.

The valence and conduction bands of the graphene layer touch each other only at the K and K' points in the Brillouin zone, as shown in Figure 6a. Thus, depending on whether the cutting lines for a given nanotube cross the K and K' points or not, this particular nanotube is expected to show either metallic (do cross) or semiconducting (do not cross) behavior. This remarkable property of carbon nanotubes being either metallic or semiconducting, depending on their geometrical structure, was first predicted theoretically[19, 20] based on the zone-folding scheme for the electronic band structure of carbon nanotubes and later was confirmed experimentally, as discussed in Section 3.2.

To determine whether a given nanotube is metallic or semiconducting, let us consider its cutting lines in the fully reduced representation and check to see whether the projection of the vector $\mathbf{K}$ pointing toward the nearest K point in the Brillouin zone, $\mathbf{K} = (2\pi/(\sqrt{3}a), 2\pi/(3a))$, in the $\mathbf{K}_1$ direction contains an integer (metallic) or a fractional (semiconducting) number of vectors $\mathbf{K}_1$. Using the expression for the vector $\mathbf{K}_1$ derived in Section 2.1.3, one can easily find that $(\mathbf{K} \cdot \mathbf{K}_1)/(\mathbf{K}_1 \cdot \mathbf{K}_1) = (2n + m)/3$. That is, carbon nanotubes could be either metallic or semiconducting, depending on whether $2n + m$ is divisible by 3 or not, or, equivalently, whether $n - m$ is divisible by 3 or not.

The cutting lines in the vicinity of the K point are shown in Figure 7 for three different cases, $n - m = 3\ell$, $n - m =$

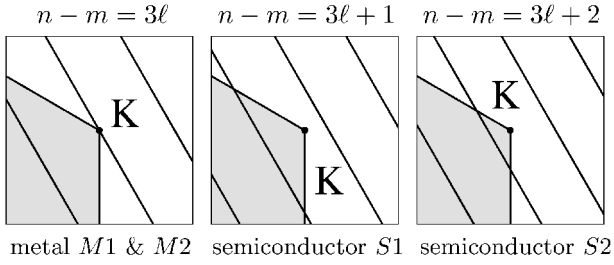

Fig. 7. Three different configurations of the cutting lines in the vicinity of the K point. The first configuration $n - m = 3\ell$ corresponds to the case of metallic nanotubes of both $M1$ and $M2$ types, and the last two configurations, $n - m = 3\ell + 1$ and $n - m = 3\ell + 2$, to the case of semiconducting nanotubes of types $S1$ and $S2$, correspondingly.

$3\ell + 1$, and $n - m = 3\ell + 2$, where ℓ is an integer. The first case $n - m = 3\ell$ corresponds to the cutting line crossing the K point, resulting in metallic behavior, as discussed above, and the other two cases, $n - m = 3\ell + 1$ and $n - m = 3\ell + 2$ (or, equivalently, $n - m = 3\ell \pm 1$ in a different notation), correspond to the K point being located at one-third and at two-thirds of the distance between two adjacent cutting lines, resulting in semiconducting behavior, since the cutting lines do not go through the K and K' points. We thus conclude that the number of semiconducting nanotubes is roughly twice that of metallic nanotubes.

The two cases of semiconducting nanotubes, $n - m = 3\ell + 1$ and $n - m = 3\ell + 2$, are also different from each other, depending on which side of the K point in the unfolded 2D Brillouin zone of the nanotube the first VHS in the DOS appears. We classify these two types of semiconducting nanotubes as $S1$ and $S2$, in accordance with the number $(n - m - 3\ell)$ being equal to either 1 or 2. In a similar fashion, we can classify metallic nanotubes by what ratio the K point divides the cutting line in the $\mathbf{K}_1$-extended representation. By projecting the vector $\mathbf{K}$ on the direction $\mathbf{K}_2$, one can find $(\mathbf{K} \cdot \mathbf{K}_2)/(\mathbf{K}_2 \cdot \mathbf{K}_2) = m/d_R$. Thus, we can classify metallic nanotubes as $M1$ and $M2$ for $d_R = d$ and $d_R = 3d$, correspondingly (see Section 2.1.1). For $M1$ metallic nanotubes, $m/d_R = m/d$ is an integer and therefore the K point appears at the wave vector $k = 0$ in the 1D Brillouin zone of the nanotube (the Γ point). For $M2$ metallic nanotubes, $m/d_R = (m/d)/3$ is one-third of an integer, and therefore the K point appears at the wave vector $k = \pm(2/3)\ (\pi/|\mathbf{T}|)$ in the 1D Brillouin zone of the nanotube (two-thirds of the distance from the central Γ point to the edge of the 1D Brillouin zone).[2] Whereas armchair nanotubes (n,n) are always $M2$ type metallic, and zigzag nanotubes can be either $M1$ type metallic $(3\ell, 0)$ or $S1$ type $(3\ell + 1, 0)$ or $S2$ type $(3\ell + 2, 0)$ semiconducting, chiral nanotubes can be of each of the four types, $M1$, $M2$, $S1$, or $S2$.

Using the results on the relative positions of the cutting lines with respect to the K point and utilizing the linear isotropic dispersion relations for electrons around the K point, we can identify approximate values for the energies at which VHSs appear in the DOS of metallic and semiconducting nanotubes. The values of these approximate energies are given by $E = \pm(\jmath/\sqrt{3})\gamma_0 a/d_t$, where $\jmath = 1, 2, 4, 5, 7, 8, \ldots$ for both $S1$ and $S2$ semiconducting nanotubes and $\jmath = 3, 6, \ldots$ for both $M1$ and $M2$ metallic nanotubes. These calculations result in an estimate for the band gap, $E_g = (2/\sqrt{3})\gamma_0 a/d_t$, for semiconducting nanotubes of both the $S1$ and $S2$ types. The actual positions of the VHSs in the DOS, however, may deviate substantially from these simple expressions because of the anisotropy in the electronic dispersion relations around the K point, as expressed by the electronic trigonal warping effect,[14] which shifts the VHS energies of $S1$ and $S2$ semiconducting nanotubes in opposite directions.

Furthermore, curvature effects, which are especially pronounced for small-diameter nanotubes, further shift the VHS energies away from these simple formulas. Hybridization of the σ and π orbitals caused by the curvature of the nanotube wall results in mini-band gaps opening up at the Fermi level of metallic nanotubes.[21] The mini-band gap width is inversely proportional to the square of the nanotube diameter[21] and depends on the nanotube chirality, being a maximum for zigzag nanotubes and vanishing for armchair nanotubes.[22] Thus, among all $M1$ and $M2$ type metallic nanotubes, only armchair nanotubes ($M2$ type) are expected to be true metals, while $M1$ and $M2$ nanotubes with other chiralities are instead quasimetals or small gap semiconductors. The curvature-induced mini-band gaps are much smaller in magnitude than the band gaps of $S1$ and $S2$ type semiconducting nanotubes. For example, the mini-band gap width for an $M1$ type zigzag nanotube (15, 0) of diameter $d_t = 1.17$ nm is about 0.03 eV, whereas the band gaps of $S1$ and $S2$ type semiconducting nanotubes of similar diameters are about 0.6 eV.[21] In spite of mini-band gaps opening up at the Fermi energy, we will continue to use the term "metallic nanotubes" for $M1$ and $M2$ type nanotubes in this article, since this convention is also commonly used in the literature, because the mini-gaps have a magnitude of about the thermal energy $k_B T$ at room temperature and are generally much smaller than the laser excitation energy in optical spectroscopy.

2.4. Electronic Density of States

The presence of VHSs in the DOS of carbon nanotubes has a great impact on their physical properties, such as transport processes, optical absorption, electron-phonon interaction, etc. Generally, a significant enhancement in the system response is observed when the excitation energy for the probe matches the VHSs in the DOS in the valence and conduction bands of the nanotube. For example, optical absorption is strongly enhanced when the photon energy is in resonance with the allowed transition between two VHSs in the valence and conduction bands. This enhancement is generally interpreted as being due to the extremely high

nanotube joint density of electronic states (JDOS, i.e., the DOS as a function of the transition energy between valence and conduction band states) at the photon energy (see Fig. 2). In this section, we consider the resonance of a photon with a VHS in the JDOS from the point of view of the cutting lines.

A photon of a given energy preferentially excites those electronic states that have a transition energy between the valence and conduction bands equal to the photon energy. These electronic states lie along equi-energy contours, which form distorted circles exhibiting threefold symmetry around the K and K' points in the Brillouin zone of the graphene layer.[14] In the case of nanotubes, only allowed electronic states, which lie at the intersections of the equi-energy contour and the cutting lines, may participate very strongly in the optical absorption. In the *resonance* case, when the photon energy matches the transition energy E_{ii} between the two VHSs E_i^v and E_i^c in the valence and conduction bands (or, in other words, the VHS E_{ii} in the JDOS), the equi-energy contour corresponding to the photon energy touches one of the cutting lines tangentially, as shown in Figure 8a.

However, the *resonance* case of Figure 8a is rarely satisfied in practice, and we rather have what is called the *preresonance* condition, where the equi-energy contour is slightly shifted in either direction from the point where it would have been tangential to the cutting line at the cross point of the contour and the line, as in Figure 8a. The two *preresonant* cases are shown in Figure 8b and c, where the equi-energy contour is shifted from the VHS in two opposite directions by an energy δE. When the photon energy increases above the VHS, the number of resonant states, shown by the bold black lines in Figure 8c, decreases gradually, whereas for the photon energy decreasing below the VHS, as shown in Figure 8b, there are no resonant states present. We refer to the resonant states as *hard-resonant* (Fig. 8a) and *soft-resonant* (Fig. 8c), depending on whether the photon energy matches or exceeds the VHS, respectively, to emphasize the decrease in the number of resonant states with increasing photon energy above the VHS.

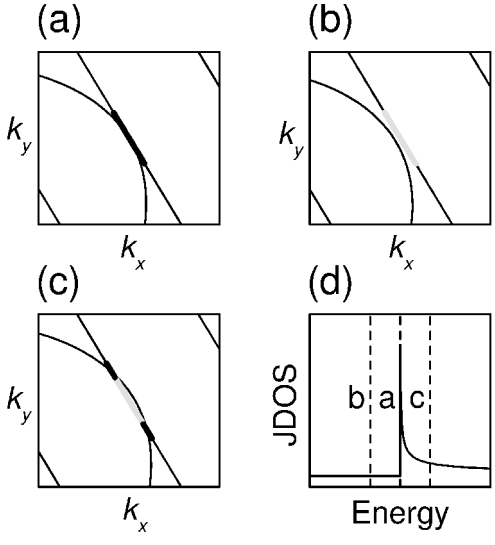

Fig. 8. (a) The resonance condition $E_{photon} = E_{ii}$ and two *preresonance* conditions (b) $E_{photon} = E_{ii} - \delta E$ and (c) $E_{photon} = E_{ii} + \delta E$. (d) JDOS profile of the VHS E_{ii}. The three dashed lines labeled a, b, and c denote the photon energies from (a) to (c), as labeled in the figure (see text for a more detailed discussion of preresonant conditions).

When the photon energy does not exactly match the VHS, contributions to the optical absorption may come not only from the soft-resonant electronic states, but also from electronic states at or close to the VHS. Although these states, shown by the bold gray lines in Figure 8b and c, are not exactly in resonance with the photon energy, they still can contribute significantly to the optical absorption due to the extremely high DOS at the VHS. We refer to these states as *preresonant.* Whereas preresonant electronic states are the only states that contribute to optical absorption in the case in Figure 8b when the photon energy is below the VHS (see bold gray lines in Fig. 8b), there are both types of electronic wave vectors, preresonant and soft-resonant, in the case in Figure 8c when the photon energy lies above the VHS (see bold gray and black bold lines in Fig. 8c).

The appearance of an additional group of soft-resonant wave vectors contributing to the optical absorption for the preresonance condition of the type in Figure 8c compared with the preresonance condition of the type in Figure 8b results in a line shape change and a broadening of the spectral features in the case of the preresonance condition of the type in Figure 8c when the photon energy exceeds the VHS. The soft-resonant states also result in an *asymmetry* of the JDOS profile of the VHS, decreasing either gradually or sharply on the two different sides of the VHS, and in an asymmetry of the resonant window for the optical absorption and for the Raman scattering. The calculated resonant window for the Raman scattering shows a significant asymmetry, reaching half of its maximum value for the laser energy 0.02 eV below and 0.05 eV above the resonant energy at which the scattering intensity reaches its maximum value, so that the resonant window extends further out from the resonant energy for the case in Figure 8c than for the case in Figure 8b (see Section 3.1).

A JDOS profile in the vicinity of the VHS generated by the cutting lines from Figure 8a to c is shown in Figure 8d, where the three dashed lines correspond to the three different energies of the equi-energy contours shown in Figure 8a to c, the dashed lines b and c show preresonance conditions, and the dashed line a shows an exact resonance. We note that the JDOS profile of the VHS is asymmetric, indicating the appearance of soft-resonant states when the photon energy exceeds the VHS, as follows from analysis of the crossing points between the cutting line and various equi-energy contours. Figure 8d provides a simplified representation of the preresonance conditions pictured in Figure 8b and c, but it loses important information about

the distribution of the resonant wave vectors. An analysis of the optical absorption in a 1D system using the JDOS profile shown in Figure 8d is suitable for rough predictions of the behavior of the spectral features, whereas a detailed analysis must involve consideration of the resonant wave vectors themselves, and the nature of the resonant and preresonant states, shown in Figure 8a to c. For example, the two different types of electronic states that appear in Figure 8c, soft-resonant (black bold lines) and preresonant (bold gray lines), correspond to two different dashed lines in Figure 8d labeled *c* and *a*, respectively, yet the photon energy corresponds to the dashed line *c* only, which makes it difficult to analyze the preresonance condition *c* from the JDOS profile alone, without the use of cutting lines.

2.5. Phonon Modes

The phonon modes of carbon nanotubes can be treated in a fashion similar to what has been used to describe the electronic dispersion relations by applying the zone-folding scheme to the 2D phonon dispersion relations of the graphene layer. The phonon dispersion relations of the graphene layer can be calculated within a force constant model[2] or by tight-binding[23] or *ab initio*[24] methods. In the force constant model, interatomic forces are represented by spring constants, and interactions up to the third nearest neighbor in the graphene layer must be taken into account to consider the curvature effects, whereas interactions up to the fourth nearest neighbor are required to adequately describe atomic motion for the different phonon modes of the graphene layer.[2]

The phonon dispersion relations of the graphene layer can be measured along high-symmetry directions in the Brillouin zone by electron energy loss spectroscopy[25] and by inelastic neutron scattering.[26] The force constants up to the fourth nearest neighbor were fitted to the phonon frequencies measured by inelastic neutron scattering in graphite.[26] These force constants were refitted recently, including the frequencies measured by resonance Raman spectroscopy on different graphitic materials.[27] Resonance Raman scattering is sensitive to the regions around the high-symmetry points Γ and K in the first Brillouin zone, whereas inelastic neutron scattering and electron energy loss spectroscopy probe primarily the high-symmetry directions ΓM and ΓK, so that the different methods provide complementary information on the phonon mode frequencies and the force constants. Furthermore, Raman scattering by photons can be used to probe the phonon modes in microscopic quantities of material, up to individual nanotubes, whereas neutron scattering and electron scattering can only be observed in bulk crystals.

However, resonance Raman spectroscopy (RRS) in various graphitic materials is only selective with respect to the distance from the high-symmetry points Γ and K in the Brillouin zone, and RRS in sp^2 carbons and in SWNT bundles averages out the direction of the phonon wave vector from the Γ or K points. With the use of recent advances in resonance Raman scattering from *individual* SWNTs,[15] the anisotropy in the phonon dispersion relations of the graphene layer around the high-symmetry point K could be reconstructed by zone-unfolding from the phonon modes of individual nanotubes.[28] The four nearest-neighbor force constants were refitted for the phonon anisotropy (also called the *phonon* trigonal warping effect, by analogy with the use of trigonal warping to denote the anisotropy in the *electronic* dispersion relations of the graphene layer[14]) to be incorporated into the force constant model.[28] As an alternative approach, the force constants can be derived from *ab initio* calculations of the phonon modes.[24] At the present time, there are discrepancies between the force constants fitted to experiments and the force constants derived from *ab initio* calculations, as described above. It is expected that these discrepancies will be eliminated with time, as the experimental techniques become more precise and *ab initio* methods become more accurate.

Two atoms A and B in the unit cell of the graphene layer (see Fig. 3) give rise to six phonon modes, because of the three degrees of freedom per atom. Superimposing the N cutting lines in the $\mathbf{K}_1$-extended representation on the six phonon frequency surfaces in the reciprocal space of the graphene layer, according to the zone-folding scheme as described in Section 2.2, yields $6N$ phonon modes for each carbon nanotube. The $6\,(N/2 - 1)$ pairs of the phonon modes arising from the cutting lines of the indices μ and $-\mu$, where $\mu = 1, \ldots, (N/2 - 1)$, are expected to be doubly degenerate, similar to the case of the electronic subbands discussed in Section 2.3, whereas the 12 phonon modes arising from the cutting lines of the indices $\mu = 0$ and $\mu = N/2$ are nondegenerate, so that the total number of distinct phonon branches is $3\,(N + 2)$. For our sample (4, 2) nanotube, there are 90 distinct phonon branches.

Spikes appear in the density of phonon states of the carbon nanotube, similar to the spikes (VHSs) appearing in the electronic DOS discussed in Section 2.4, except for a much larger number of spikes in the phonon DOS than in the electronic DOS, due to the larger number of phonon modes relative to the number of electronic bands, and the more complex structure of the dispersion relations for phonons than for electrons in the graphene layer. However, the spikes in the phonon DOS do not play such an important role in experimental outcomes as the spikes in the electronic DOS because of the symmetry restrictions.

Among the large number of phonon modes in carbon nanotubes, only 15 or 16 are Raman-active and only 7, 8, or 9 are infrared-active, as predicted by group theory,[6] yet some claim an even smaller number of optically active modes.[29] Further details about the selection rules for the phonon modes are discussed in Section 2.6. The phonon dispersion relations of the graphene layer in the force constant model are shown in Figure 9a along with the cutting

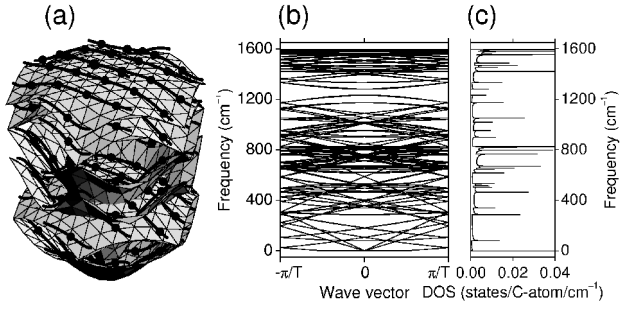

Fig. 9. (a) The phonon dispersion relations of the graphene layer in the first Brillouin zone calculated with the force constants fitted to the Raman scattering data for various graphitic materials.[27] Solid curves show the cutting lines for the (4, 2) nanotube in the fully reduced representation. Solid dots show the ends of the cutting lines in the $\mathbf{K}_1$-extended representation. (b) Phonon modes for the (4, 2) nanotube obtained by zone-folding from (a). (c) Density of states for the phonon modes shown in (b).

lines for our (4, 2) sample nanotube in the fully reduced representation. The resulting phonon modes and the phonon density of states for the (4, 2) nanotube are shown in Figure 9b and c, correspondingly.

The zone-folding scheme, as described in Section 2.2, neglects the curvature of the nanotube wall, as was already mentioned in Sections 1.2 and 2.3. Meanwhile, the curvature couples the in-plane and out-of-plane phonon modes of the graphene layer to each other, especially affecting the low-frequency acoustic phonon modes. Among the three acoustic phonon modes of the graphene layer, only one of the two in-plane modes results in the acoustic phonon mode of the nanotube corresponding to the vibrational motion along the nanotube axis. The two other in-plane and out-of-plane acoustic phonon modes give rise to the twisting mode (TWM, the vibrational motion in the circumferential direction of the nanotube) and to the radial breathing mode (RBM, the vibrational motion in the radial direction of the nanotube), correspondingly, and the two related acoustic phonon modes of the nanotube (the vibrational motion in two orthogonal directions perpendicular to the nanotube axis) can be constructed as linear combinations of the RBM and TWM modes.[2]

The zone-folding scheme predicts zero frequencies for the perfectly symmetric RBM and TWM phonon modes of the nanotube at the center of the Brillouin zone, since they arise from the acoustic phonon modes of the graphene layer. Meanwhile, the frequency of the perfectly symmetric RBM is inversely proportional to the nanotube diameter, varying from around 100 to 250 cm^{-1} for typical diameters of 1 to 2 nm, as was first predicted within the force constant model[26] and then confirmed by resonance Raman scattering measurements[30] and by *ab initio* calculations,[31] which also revealed a weak dependence of the RBM frequency on the nanotube chirality. The zone-folding scheme is thus not accurate for the low-frequency phonon modes (zone-center acoustic modes), although it does provide reliable results for the high-frequency phonon modes (optical modes), as confirmed by *ab initio* calculations.[32] To avoid the limitations of the zone-folding scheme for the low-frequency phonon modes, the force constant model can be used directly for the nanotube by constructing and solving the $6N \times 6N$ dynamic matrix for the unit cell of the nanotube, instead of using the 6×6 dynamic matrix for the unit cell of the graphene layer with consequent zone-folding.[2] Alternatively, the first-principles methods can be used instead of the force constant models to calculate the phonon modes, yet the size of the unit cell cannot be too large for *ab initio* methods. Therefore, *ab initio* calculations are currently limited to achiral nanotubes and to only a few chiral nanotubes with relatively small unit cells. Moreover, the accuracy of the experiments significantly exceeds what *ab initio* methods can currently do.

In the discussion above, we use the zone-folding scheme with the cutting lines in the $\mathbf{K}_1$-extended representation for our analysis of the phonon modes in carbon nanotubes. As we show in Section 2.2.2, the momentum change along the nanotube axis can be equally treated as the symmetry change in the circumferential direction under certain conditions, so that we can use the cutting lines in the fully reduced representation and even in the $\mathbf{K}_2$-extended representation for the zone-folding scheme of the phonon modes (see Sections 2.2.1 and 2.2.3, respectively). The latter was used to calculate the phonon modes of the two chiral nanotubes within a symmetry-based force constant model.[33] For the (14, 5) nanotube, $d = 1$, $d_R = 3$, $N = 194$, $(p,q) = (3,-4)$, $M = 71$, and $Q = 1$, so that there is a single cutting line of length $(N/Q)\mathbf{K}_2 = 194\mathbf{K}_2$ in the $\mathbf{K}_2$-extended representation, resulting in $6Q = 6$ phonon modes and a phonon wave vector that varies from $-194\pi/|\mathbf{T}|$ to $194\pi/|\mathbf{T}|$ (see Fig. 3 of Ref. 33). For the (12, 8) nanotube, $d = 4$, $d_R = 4$, $N = 152$, $(p, q) = (1, -1)$, $M = 20$, and $Q = 4$, so that there are four cutting lines of length $(N/Q)\mathbf{K}_2 = 38\mathbf{K}_2$ in the $\mathbf{K}_2$-extended representation, resulting in $6Q = 24$ phonon modes, and the phonon wave vector here varies from $-38\pi/|\mathbf{T}|$ to $38\pi/|\mathbf{T}|$ (see Fig. 4 of Ref. 33). In contrast, for the (10, 10) armchair nanotube, $d = 10$, $d_R = 30$, $N = 20$, $(p, q) = (1, 0)$, $M = 10$, and $Q = 10$, so that there are 10 cutting lines of length (N/Q) $\mathbf{K}_2 = 2\mathbf{K}_2$ in the $\mathbf{K}_2$-extended representation, resulting in $6Q = 60$ phonon modes, and the phonon wave vector varies from $-2\pi/|\mathbf{T}|$ to $2\pi/|\mathbf{T}|$, whereas in the $\mathbf{K}_1$-extended representation, there are 20 cutting lines of length $\mathbf{K}_2$ resulting in 120 phonon modes, and the phonon wave vector is this case varies from $-\pi/|\mathbf{T}|$ to $\pi/|\mathbf{T}|$. Thus we can see that the $\mathbf{K}_2$-extended representation of the cutting lines for the (10, 10) armchair nanotube is not so much prolonged in the $\mathbf{K}_2$ direction when compared with the $\mathbf{K}_1$-extended representation (only twice), unlike the situation for a (14, 5) nanotube, where the two extended representations are strongly prolonged in the two orthogonal directions $\mathbf{K}_1$ and $\mathbf{K}_2$.

2.6. Selection Rules

In spite of the large number of electronic and phonon subbands in carbon nanotubes (see Figs. 6 and 9), very few of the subbands participate in infrared absorption and Raman scattering because of symmetry restrictions. The selection rules governing the above-mentioned processes are commonly derived from group theory. At the same time, the selection rules are closely related to the concept of cutting lines, and they can easily be obtained from the zone-folding procedure. In the present section, we discuss the selection rules for the electron-photon interaction and for the electron-phonon interaction in SWNTs.

Selection rules are required for a deeper understanding of the resonance Raman scattering process in carbon nanotubes (see Section 3), for the interpretation of infrared spectra in carbon nanotubes,[34] for optical absorption,[35] for luminescence measurements,[36] and for many other aspects of nanotube science. To make the discussion of the selection rules clearer for the reader, we plot in Figure 10 the schematic band diagram of the nanotube in the unfolded 2D Brillouin zone. Although the cutting lines in the $\mathbf{K}_1$-extended representation, shown in Figure 10 by the dashed line segments, correspond to the simple case of a zigzag metallic nanotube, our discussion is generally applicable to both metallic and semiconducting nanotubes of all chiralities and diameters. The electronic subbands arising from these cutting lines are shown in Figure 10 by solid curves of parabolic shape, each labeled by three symbols (C/V for conduction and valence bands, the VHS index or the cutting line index, and L/U for the two opposite directions *K*M and *K*Γ from the *K* and *K*′ points; see figure caption for details), and the corresponding electronic VHSs are shown by solid dots.

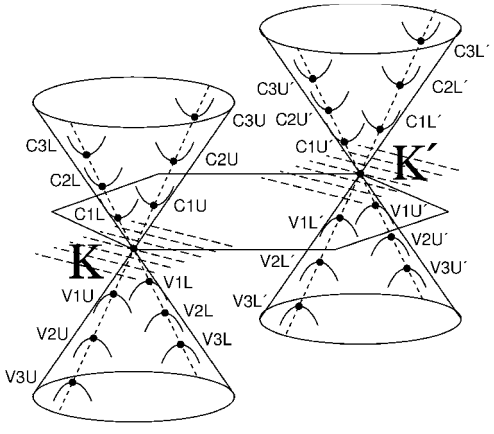

Fig. 10. The electronic subbands for zigzag metallic nanotubes in the vicinity of the K and K′ (near the Fermi energy) points in the first Brillouin zone. The VHSs are labeled by three symbols; the first denotes valence or conduction band (C/V), the second denotes the VHS index counted away from the Fermi energy or the cutting-line index counted away from the *K* and *K*′ points, and the third denotes the lower and upper energy components (L/U) due to the trigonal warping[14] splitting in the energy of the electronic VHSs for metallic SWNTs.

For light propagating perpendicular to the graphene layer (the most commonly used geometry), the polarization vector is always parallel to the graphene layer, so that light absorption and emission for a graphene layer do not depend on the polarization of the light beam. Absorption or emission of a photon in the optical frequency range in the graphene layer involves an electronic transition between the valence and conduction bands in the vicinity of the *K* or *K*′ point. In the dipole approximation, the optical transition is *vertical*, that is, the electronic wave vector does not change when the electron is scattered by the photon with polarization parallel to the graphene layer.

Similarly, the optical transition in the nanotube is vertical within the 1D Brillouin zone, that is, the electronic wave vector along the nanotube axis (along the $\mathbf{K}_2$ vector in the unfolded 2D Brillouin zone) does not change. In contrast to the case of the graphene layer, the polarization vector can be either parallel or perpendicular to the nanotube axis for light propagating perpendicular to the substrate on which the nanotubes lie. The interband electronic transitions for light polarized perpendicular to the nanotube axis are suppressed by the depolarization effect.[37–39] The dipole selection rules tell us that the optical transition in the nanotube conserves the electronic subband index (the cutting line index) for the light polarized parallel to the nanotube axis.[37, 40] Conservation of both the 1D wave vector and the subband index implies conservation of the 2D wave vector in the Brillouin zone of the graphene layer (unfolded Brillouin zone of the nanotube). For example, if an electron in the valence subband V2U of Figure 10 (see the parabolic curve in Figure 10 labeled V2U) absorbs a photon, the electron goes vertically to the conduction subband C2L. If the electron now starts from the VHS in the valence subband V2U (see the solid dot on the subband V2U in Fig. 10), this electron goes to the VHS in the conduction subband C2L, and the optical absorption is enhanced substantially because of the extremely high DOS at the VHSs in the valence and conduction subbands, V2U and C2L. Consequently, the optical absorption or emission rate in nanotubes is determined by the electronic states at the VHSs and in the vicinity of the VHSs (see discussion of the VHS shape and resonant vs. preresonant states in Section 2.4). Note that the optical transition occurs only between two VHSs in the valence and conduction subbands within *the same* cutting line μ because of the dipole selection rules.

The dipole selection rules allow us to consider the VHSs in the JDOS (joint density of electronic states; see Section 2.4) rather than the VHSs in the valence and conduction bands separately. In the definition of the JDOS (see Section 2.4), the dipole selection rules are implied, that is, only vertical transitions between the valence and conduction subbands within the same cutting line μ are taken into account. This definition of the JDOS results in one and only one VHS in the JDOS profile for each pair of VHSs in the DOS. For example, the pair of VHSs V2U and C2L in

Figure 10 results in a VHS in the JDOS. The VHSs in the DOS associated with the valence and conduction subbands are commonly labeled $E_{\mu}^{(v)}$ and $E_{\mu}^{(c)}$ (see Fig. 1), or $E_{i}^{(v)}$ and $E_{i}^{(c)}$, where μ is the cutting-line index in the unfolded 2D Brillouin zone (or the subband index in the folded 1D Brillouin zone), with μ varying from $1 - N/2$ to $N/2$ (see Fig. 4), and i is the VHS index on the energy scale, which increases in number as we move away from the Fermi level $E = 0$. We will use both indices μ and i, respectively, depending on whether we consider the VHSs in the unfolded 2D Brillouin zone (see Figs. 1a and 10) or on the energy scale (see Figs. 1b and 6c). Note that although there is a direct correspondence between the indices i and μ for achiral nanotubes, such as zigzag metallic nanotubes, shown in Figure 10, for which we have $i = ||\mu| - N/3|$, there is generally no such simple relation between i and μ for chiral nanotubes. For our (4, 2) sample nanotube, the VHS index i varying from 1 to 6 corresponds to the cutting line index μ taking values ± 9, ± 10, 14, ± 2, ± 1, and 0, respectively, whereas the μ values from ± 3 to ± 8 and from ± 11 to ± 13 have no i values associated with them (no VHSs), as explained in Section 2.3. The VHSs in the JDOS are labeled by $E_{\mu\mu}$ for the transition energy between the VHSs $E_{\mu}^{(v)}$ and $E_{\mu}^{(c)}$ in the DOS, or by E_{ii} for the transition energy between the VHSs $E_{i}^{(v)}$ and $E_{i}^{(c)}$ in the DOS. It is quite common in spectroscopic studies of carbon nanotubes to plot the transition energies for the VHSs in the JDOS, E_{ii}, as a function of the nanotube diameters, d_t, for each (n,m) SWNT (see Fig. 16b in Section 3.2), to identify the resonance nanotubes and to analyze their optical and Raman spectra (so-called Kataura plot).[41]

The dipole selection rules predict vertical optical transitions within the same cutting line μ for light polarized parallel to the nanotube axis. Direct calculations of the optical transition matrix elements confirm the dipole selection rules for light polarized parallel to the nanotube axis.[42] For light polarized perpendicular to the nanotube axis, both the dipole selection rules[37, 40] and direct calculations of the optical transition matrix elements[42] indicate that the interband optical transitions can only happen between the two adjacent cutting lines in the $\mathbf{K}_1$-extended representation. For example, if an electron in the valence subband V2U in Figure 10 absorbs a photon polarized perpendicular to the nanotube axis (i.e., polarized along the $\mathbf{K}_1$ vector), it can scatter to one of the two conduction subbands, either C1L or C3L, depending on the photon frequency and on the interband transition energies $E_{2,1}$ and $E_{2,3}$. Similarly, if an electron in the conduction subband C2L emits a photon polarized perpendicular to the nanotube axis, it can scatter to the V1U or V3U valence subband. This implies a different set of VHSs in the JDOS for perpendicular polarization, $E_{\mu,\mu\pm 1}$, and these energies are located approximately halfway between the VHSs in the JDOS for parallel polarization, $E_{\mu\mu}$. Whereas the VHSs $E_{\mu\mu}$ can be equally indexed as E_{ii}, the VHSs $E_{\mu,\mu\pm 1}$ directly corresponds to $E_{i,i\pm 1}$ only for the case of achiral nanotubes, such as zigzag and armchair SWNTs. For chiral nanotubes, even if the cutting line μ is associated with the VHSs $E_{\mu}^{(v)}$ and $E_{\mu}^{(c)}$ in the DOS, the cutting lines $\mu \pm 1$ may produce no VHSs in the DOS (see Section 2.3). However, there still can be VHSs $E_{\mu,\mu\pm 1}$ in the JDOS, which appear at different wave vectors than for the VHSs $E_{\mu}^{(v)}$ and $E_{\mu}^{(c)}$ in the DOS, namely, at the wave vectors where the two subbands μ and $\mu \pm 1$ have the same slope.

Whereas the optical transition is vertical for light polarized parallel to the nanotube axis, it involves a wave vector change of $\pm\mathbf{K}_1$ (the distance between two adjacent cutting lines) for the perpendicular polarization. This wave vector change can be easily understood by considering an unrolled nanotube, as shown in Figure 11. When the nanotube is unrolled into the graphene layer, the light polarized parallel to the nanotube axis transforms into the light polarized parallel to the graphene layer, as shown in Figure 11a, resulting in a vertical interband optical transition in the unfolded 2D Brillouin zone, which is equivalent to the optical transition within the same subband μ in the folded 1D Brillouin zone of the nanotube, as predicted by the dipole selection rules.

However, perpendicular polarization in nanotubes becomes transformed into the in-plane and out-of-plane polarizations in the unfolded graphene layer, periodically modulated along the direction of the $\mathbf{K}_1$ vector with the period πd_t (nanotube circumference), as shown in Figure 11b. The optical transitions induced by the out-of-plane polarization are expected to be much weaker compared with those induced by the in-plane polarization and thus can be ignored, because of the much stronger in-plane interaction in the graphene layer. This implies that the light polarization in the unrolled nanotube shown in Figure 11b can be considered, as a first approximation, to be parallel to the graphene layer, with an additional phase factor describing oscillations of the in-plane polarization component, arising from the rotation of the polarization vector.[37] The phase factor is given by $\cos(\mathbf{k} \cdot \mathbf{r})$, where the wave vector $\mathbf{k}$ has the direction of $\mathbf{K}_1$ and a magnitude of $2\pi/(\pi d_t) = 2/d_t$, that is, $\mathbf{k} = \mathbf{K}_1$. By expanding $\cos(\mathbf{K}_1 \cdot \mathbf{r})$ into a sum of $\exp(i\mathbf{K}_1 \cdot \mathbf{r})$ and $\exp(-i\mathbf{K}_1 \cdot \mathbf{r})$, we obtain the two photons with wave vectors $\pm\mathbf{K}_1$ polarized parallel to the unrolled graphene layer.

The wave vector of the original photon propagating perpendicular to the nanotube axis is negligible, since the photon wave length λ (of about 1 μm) is much larger than the

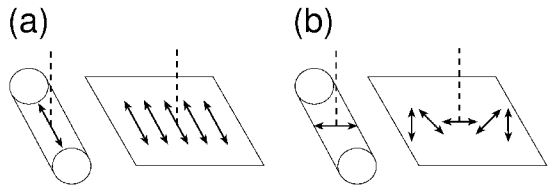

Fig. 11. Light polarization (a) parallel and (b) perpendicular to the nanotube axis, shown for both a rolled-up SWNT (left), and a SWNT unrolled into the graphene layer (right). The arrows show the light polarization vector, and the dashed lines show the light propagation direction.

tube diameter d_t (of about 1 nm). We thus are left with the two photons with wave vectors $\pm\mathbf{K}_1$ in the unrolled graphene layer. By assuming wave vector conservation in the unfolded 2D Brillouin zone for the optical transition process, we come up with the selection rules $\mathbf{k}_c = \mathbf{k}_v \pm \mathbf{K}_1$ for light absorption and $\mathbf{k}_v = \mathbf{k}_c \pm \mathbf{K}_1$ for light emission, which correspond to the electronic transition to the adjacent cutting line in the unfolded 2D Brillouin zone, or the electronic transition to the adjacent subband in the 1D Brillouin zone of the nanotube, as predicted by the dipole selection rules[37, 40] and confirmed by direct calculations of the optical transition matrix elements.[42] It is interesting to note that the photon wave vector $\pm\mathbf{K}_1$ in the unrolled graphene layer is much larger in magnitude than the photon wave vector k in free space, $K_1 = 2/d_t \gg k = 2\pi/\lambda$, because the nanotube diameter d_t is much smaller than the optical wavelength λ. Therefore, an optical photon in the unrolled graphene layer can be considered as an X-ray photon with respect to spatial considerations, yet the photon energy does not change when the nanotube is unrolled into the graphene layer. Such a "pseudo-X-ray" photon is a source for breaking the optical selection rules in the case of perpendicular polarization.

We can consider the wave vector conservation in the unfolded 2D Brillouin zone for the electron-photon interaction process to derive the dipole selection rules, as shown above. In a similar fashion, we can consider the wave vector conservation in the unfolded 2D Brillouin zone for the electron-phonon interaction process.[28] In the case of Umklapp scattering, a reciprocal lattice translation vector adds up to give wave vector conservation. This approach allows us to determine the Raman-active and infrared-active phonon modes, their polarization dependencies, and their resonance conditions, which are in excellent agreement with predictions based on group theory and experimental observations (see Section 3.3).

Let us denote an electronic state by (k, μ, α), where k is the 1D wave vector along the nanotube axis, μ is the cutting-line index or subband index, and α stands for the valence ($\alpha = v$) or conduction ($\alpha = c$) band. Similarly, a phonon state is denoted by (q, η, β), where q is the 1D wave vector, η is the cutting line index, and $\beta = 1 \ldots 6$ is the phonon mode of the graphene layer. For an electron in the initial state (k_1, μ_1, α) scattered by a phonon (q, η, β) to the final state (k_2, μ_2, α), the wave vector conservation along the nanotube axis implies that $k_2 = k_1 \mp q$, where the $\mp$ signs correspond to Stokes ($-$)/anti-Stokes ($+$) (phonon emission/absorption) processes. The selection rules for the electron-phonon interaction establish a relation between μ_1, μ_2, and η in a similar way, $\mu_2 = \mu_1 \mp \eta$, which is equivalent to momentum conservation in the unfolded 2D Brillouin zone, as discussed above. In the $\mathbf{K}_1$-extended representation of the cutting lines, the wave vectors of the initial electron and of the phonon, k_1 and q, respectively, vary from $-\pi/T$ to π/T, and their cutting-line indices, μ_1 and η, vary from $1 - N/2$ to $N/2$. The wave vector k_2 and the cutting line index μ_2 of the final electron obtained from the selection rules, $k_2 = k_1 \mp q$ and $\mu_2 = \mu_1 \mp \eta$, can fall beyond the limits of the $\mathbf{K}_1$-extended representation, $-\pi/T < k_2 \leq \pi/T$ and $1 - N/2 \leq \mu_2 \leq N/2$. In such a case, k_2 and μ_2 should be translated, respectively, to the $\mathbf{K}_1$-extended representation with the vectors $N\mathbf{K}_1$ and $\mathbf{K}_2 - M\mathbf{K}_1$ (see Section 2.2.2 and Table I). Similarly, in the $\mathbf{K}_2$-extended representation of the cutting lines, the wave vectors k_1 and q are defined within the range from $-(N/Q)\pi/T$ to $(N/Q)\pi/T$, the cutting-line indices μ_1 and η are defined within the range from $1 - Q/2$ to $Q/2$, and k_2 and μ_2 can be translated, respectively, to the $\mathbf{K}_2$-extended representation with the vectors $(N/Q)\mathbf{K}_2$ and $Q\mathbf{K}_1 - W\mathbf{K}_2$ (see Sect. 2.2.3 and Table I). The selection rules do not depend on the cutting-line representation, thereby providing the same results for physical observables for both the $\mathbf{K}_1$-extended and $\mathbf{K}_2$-extended representations. This means that we can either (i) translate (k_1, μ_1, α) and (q, η, β) to the $\mathbf{K}_1$-extended representation, calculate (k_2, μ_2, α) from the selection rules, and then translate the calculated (k_2, μ_2, α) to the $\mathbf{K}_1$-extended representation if needed; or (ii) translate (k_1, μ_1, α) and (q, η, β) to the $\mathbf{K}_2$-extended representation, calculate (k_2, μ_2, α) from the selection rules, and then translate the calculated (k_2, μ_2, α) to the $\mathbf{K}_2$-extended representation if needed; and in both cases (i) and (ii) we come up with *the same* final electronic state (k_2, μ_2, α) in the two different representations. Note that a single representation, either the $\mathbf{K}_1$-extended or the $\mathbf{K}_2$-extended representation, should be used for the whole problem.

To illustrate the usage of the selection rules introduced for the electron-photon and electron-phonon interaction processes, we consider the first-order resonance Raman scattering process in carbon nanotubes.[15] The first-order Raman scattering process involves the following steps: light absorption, scattering by a phonon, and light emission by an electron. The Raman signal is sufficiently enhanced when the electron scatters between the two VHSs in the DOS, so that we can consider only the transitions between the two VHSs in the DOS as a first approximation. By utilizing the selection rules introduced above, we come up with the following five classes for the allowed first-order resonance Raman scattering processes between the VHSs $E_\mu^{(v)}$ and $E_{\mu'}^{(c)}$, according to Ref. 43,

$$\begin{aligned}
&\text{(I)} && E_\mu^{(v)} \xrightarrow{Z} E_\mu^{(c)} \xrightarrow{A} E_\mu^{(c)} \xrightarrow{Z} E_\mu^{(v)} \\
&\text{(II)} && E_\mu^{(v)} \xrightarrow{X} E_{\mu\pm1}^{(c)} \xrightarrow{A} E_{\mu\pm1}^{(c)} \xrightarrow{X} E_\mu^{(v)} \\
&\text{(III)} && E_\mu^{(v)} \xrightarrow{Z} E_\mu^{(c)} \xrightarrow{E_1} E_{\mu\pm1}^{(c)} \xrightarrow{X} E_\mu^{(v)} \\
&\text{(IV)} && E_\mu^{(v)} \xrightarrow{X} E_{\mu\pm1}^{(c)} \xrightarrow{E_1} E_\mu^{(c)} \xrightarrow{Z} E_\mu^{(v)} \\
&\text{(V)} && E_\mu^{(v)} \xrightarrow{X} E_{\mu\pm1}^{(c)} \xrightarrow{E_2} E_{\mu\mp1}^{(c)} \xrightarrow{X} E_\mu^{(v)}
\end{aligned} \tag{3}$$

where A, E_1, and E_2 denote phonon modes of different Γ-point symmetries of the cutting lines $\mu = 0$, $\mu = \pm1$, and $\mu = \pm2$, respectively,[2, 44] as shown in Figure 12. The XZ plane is parallel to the substrate on which the nanotubes

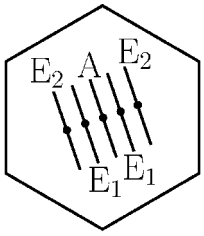

Raman-active modes		Basis functions	
Chiral	Achiral		
A	A_{1g}	$X^2 + Y^2$	Z^2
E_1	E_{1g}	XZ	YZ
E_2	E_{2g}	$X^2 - Y^2$	XY

Fig. 12. The Raman-active modes of A, E_1, and E_2 symmetries and the corresponding cutting lines $\mu = 0$, $\mu = \pm 1$, and $\mu = \pm 2$ in the unfolded 2D Brillouin zone. The Γ points of the cutting lines are shown by solid dots. The table gives irreducible representations and basis functions for the Raman-active modes according to group theory. The *Z* axis is parallel and the *XY* plane is perpendicular to the nanotube axis.[2, 44]

lie, the *Z* axis is directed along the nanotube axis, and the *Y* axis is directed along the light propagation direction, so that the *Z* and *X* in Eq. (3) stand for the light polarized parallel and perpendicular to the nanotube axis, respectively. As an example, let us consider one of the five processes given by Eq. (3), namely process (III), in the unfolded 2D Brillouin zone shown in Figure 10. When an electron at the VHS V2U absorbs a photon polarized parallel to the nanotube axis, it goes to the VHS C2L (vertical optical transition). Then the electron from the VHS C2L is scattered to the VHS C1L by a phonon of E_1 symmetry (a phonon from the Γ point of the cutting line $\mu = 1$ for the Stokes process). Finally, the electron from the VHS C1L recombines with the hole from the VHS V2U, emitting a photon polarized perpendicular to the nanotube axis (optical transition to the adjacent cutting line). Such a polarization configuration of the incident and scattered light is denoted by *ZX*. The incident and scattered photons are, respectively, resonant with the two different VHSs in the JDOS, $E_{2,2}$ and $E_{2,1}$. The five processes of Eq. (3) result in different polarization configurations for different phonon modes, *ZZ* and *XX* for A, *ZX* and *XZ* for E_1, and *XX* for E_2, in perfect agreement with the basis functions predicted by group theory (see the table in Fig. 12). Also, Eq. (3) predicts *different* resonance conditions for *different* phonon modes. Whereas the A and E_1 modes can be observed in resonance with both the $E_{\mu\mu}$ and $E_{\mu,\mu\pm1}$ VHSs in the JDOS, the E_2 modes can only be observed in resonance with the $E_{\mu,\mu\pm1}$ VHSs. Experimentally observed Raman scattering spectra follow the predicted polarization configurations and resonance conditions, as we show in Section 3.3.

3. EXPERIMENTAL EVIDENCE

We select certain experimental techniques that are especially sensitive to 1D effects in carbon nanotubes for the present discussion. In this section we show that these experimental techniques confirm the validity of the concept of cutting lines and of the zone-folding scheme. We consider separately the effects of the cutting lines on (1) the electronic density of states, (2) the metallic and semiconducting properties of carbon nanotubes, and (3) resonance Raman scattering.

3.1. van Hove Singularities

One of the major impacts of zone-folding on the electronic properties of SWNTs is the appearance of VHSs in their electronic DOS at those points in the reciprocal space of the graphene layer where the cutting lines touch equi-energy contours, as explained in Section 2.4. The appearance of VHSs in the DOS implies the presence of an extremely large number of electronic states at certain values of the energy. When the excitation energy comes into resonance with one of the VHSs, the response of the system is strongly enhanced.

Scanning tunneling spectroscopy (STS) can be used for direct measurements of the local DOS profiles of SWNTs, since the normalized differential conductance $(dI/dV)/(I/V)$ (where I is the tunneling current and V is the bias voltage) is proportional to the local DOS. Combined atomic resolution scanning tunneling microscopy (STM) and STS measurements on isolated nanotubes thus reveal the local DOS profile (by STS), as well as the tube diameter d_t and the chiral angle θ (by STM) of the same nanotube. The measured local DOS profiles of isolated nanotubes demonstrate the presence of spikes identified as VHSs, and the measured energy band gap width of semiconducting nanotubes decreases with increasing tube diameter,[10] in agreement with predictions of the zone-folding scheme. When the tube diameter d_t increases, the distance between two adjacent cutting lines $|\mathbf{K}_1| = 2/d_t$ decreases, and therefore the band gap of semiconducting nanotubes $E_g = (2/\sqrt{3})\gamma_0 a/d_t$ also decreases (see Section 2.3 for details).

Atomic resolution STM measurements on isolated nanotubes allow the identification of their (n, m) indices, which can be used to construct the cutting lines and to calculate the DOS of the nanotube, according to the zone-folding procedure described in Section 2. This calculated DOS can be further compared to the local DOS profile measured by STS on the same nanotube. We show three pairs of measured and calculated DOS profiles in Figure 13 for three isolated metallic SWNTs of zigzag chiral symmetry on an Au substrate taken from Ref. 45. One can clearly see good agreement between the measured local DOS profiles (the upper curves for each (n,m)) and the calculated DOS profiles with the transfer integral $\gamma_0 = 2.6$ eV (the lower curves for each (n,m)) for the relative energies of the VHSs on the abscissa, except for the mini-band gaps in the measured local DOS profiles at the Fermi energy, circled by dashed lines in Figure 13. These mini-band gaps are induced by the curvature of the nanotube wall, as discussed in Sections 2.3 and 3.2. The experimentally measured VHSs shown in Figure 13 seem to be much broader than the VHSs calculated within the zone-folding scheme. The VHS broadening is explained by the relatively low STS

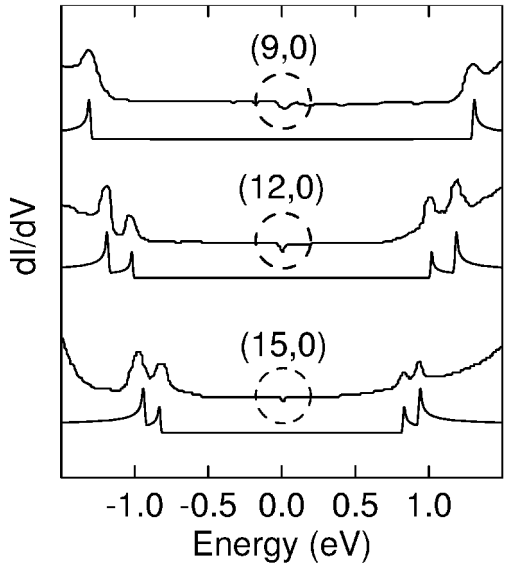

Fig. 13. Tunneling conductance data for three different metallic zigzag nanotubes on an Au substrate, taken from Ref. 45. The mini-band gap width decreases with increasing nanotube diameter d_t, as circled by dashed lines. The calculated DOS curves are shown for each nanotube under the experimental curve. The transfer integral $\gamma_0 = 2.6$ eV was used in their calculations.

resolution in energy, caused by the strong interaction of the STS tip with the nanotube. Also, charge transfer between the SWNT and the Au substrate likely occurs. The low STS energy resolution smears out the sharp VHSs in the DOS of carbon nanotubes. The sharpness of the VHSs is well known from Raman measurements,[46] which provide much higher energy resolution than other techniques, such as STS,[45] optical absorption,[35] or optical fluorescence,[36] yet suffer from low spatial resolution (the laser spot size is about 1 μm, which is approximately the same as the nanotube length). In contrast, STS is wonderful for measuring spatial resolution, so that changes in the local DOS and in the VHSs due to defects, bends, kinks, etc. can be monitored.

The VHS profiles of isolated nanotubes can be measured not only by STS but also by the Raman scattering technique. Resonance Raman spectroscopy has been shown to provide a powerful technique for the characterization of SWNTs, because of the diameter selectivity of the resonance Raman scattering process[30] and the strong electronphonon coupling under resonance conditions.[6] Recent advances in resonance Raman spectroscopy measurements on isolated SWNTs are reviewed in Ref. 15. Raman scattering from SWNTs is sufficiently enhanced when an optical transition occurs between two VHSs in the valence and conduction bands, or, equivalently, at a VHS in the joint density of electronic states (JDOS). By varying the laser excitation energy around the VHS in the JDOS, we thus expect to observe a strong enhancement in all Raman features when either the incident light of the laser or the scattered light (which is shifted from the laser line by the energy of the absorbed or emitted phonon) is in resonance with the VHS. This implies that the resonant window of the Raman feature for a given SWNT is formed by two resonances with the same VHS in the JDOS for both the incident and the scattered light.

The resonant window for the anti-Stokes process (phonon absorption) of one of the Raman features known as the radial-breathing mode (RBM), measured in Ref. 46 from an individual isolated SWNT with the laser energy varying from 1.623 eV to 1.722 eV, is shown in Figure 14. Experimentally observed Raman intensities are shown by circles and squares for two different runs over the laser energies, and the solid line indicates the theoretically predicted resonant window. The relative position of the resonant window on the abscissa is determined by the energy of the VHS in the JDOS profile, shown by the dashed line in Figure 14. Both the VHS energy E_{ii} and the VHS effective width Γ_J are found by fitting the resonant window to the experimental data, $E_{ii} = 1.655 \pm 0.003$ eV and $\Gamma_J = 0.1 - 1.0$ meV.[46] Resonance Raman spectroscopy thus provides a probe of the highest energy resolution for the VHS profiles achieved at the present time, about 1 meV, whereas other experimental techniques are not sensitive enough in the meV range resolution. For example, the STS energy resolution is lower than 10 meV (see Fig. 13).

The resonant window shown in Figure 14 by the solid line has an asymmetric shape with respect to the VHS. Within the model used for Raman line shape simulations,[46] the asymmetry of the resonant window arises from the asymmetric shape of the VHS (see Section 2.4) and from the presence of two resonances, one with the incident and one with the scattered light. Although the experimental points shown by dots and squares in Figure 14 may indicate some asymmetry of the resonant window, the signal-to-noise ratio for these experimental data is insufficient to provide a clear identification of

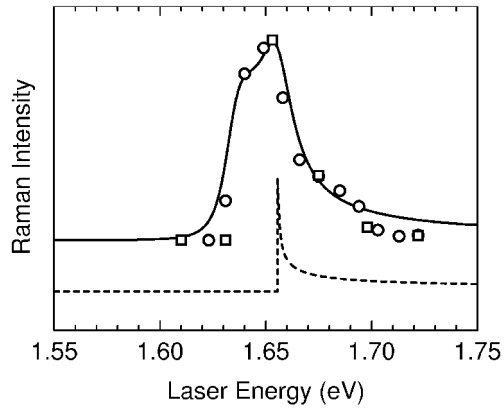

Fig. 14. Raman intensity vs. laser excitation energy for the anti-Stokes RBM feature at the 173.6 cm^{-1} Raman shift, assigned to an isolated (18, 0) SWNT on a Si/SiO_2 substrate, taken from Ref. 46. The predicted resonant window is shown by the solid curve, and the VHS in the JDOS at 1.655 eV is shown by the dashed curve. Circles and squares indicate two different runs taken with a tunable laser over the indicated laser energies.

the experimental line shape. It is expected that in the future, more precise Raman experiments will clarify the question of the experimentally observed resonant window asymmetry.

The resonant window for a first-order Raman feature, such as the RBM mode shown in Figure 14, can be calculated within third-order time-dependent perturbation theory,

$$I(E_l) = \sum_{\mathbf{k}} |K(\mathbf{k})|^2$$
$$K(\mathbf{k}) = \frac{M_{\text{opt}}^{\text{abs}}(\mathbf{k})\, M_{\text{el-ph}}^{\text{S/AS}}(\mathbf{k})\, M_{\text{opt}}^{\text{ems}}(\mathbf{k})}{(E_l - E(\mathbf{k}) - i\Gamma)\,(E_l \mp \hbar\omega_{\text{ph}} - E(\mathbf{k}) - i\Gamma)} \quad (4)$$

where $K(\mathbf{k})$ is the third-order matrix element; $\mathbf{k}$ is the wave vector of the initial electronic state; $M_{\text{opt}}^{\text{abs}}$, $M_{\text{el-ph}}^{\text{S/AS}}$, and $M_{\text{opt}}^{\text{ems}}$ are, respectively, the transition matrix elements for the optical absorption, electron-phonon interaction for either the Stokes (phonon emission) or anti-Stokes (phonon absorption) processes, and optical emission; E_l is the laser excitation energy; ω_{ph} is the zone-center phonon frequency; $E(\mathbf{k}) = E_c(\mathbf{k}) - E_v(\mathbf{k})$ is the electronic transition energy; Γ is proportional to the inverse lifetime for the scattering process; and the $\mp$ signs correspond to the Stokes($-$)/anti-Stokes($+$) processes, that is, phonon emission/absorption.[47] Electronic transitions for the light absorption/emission processes are vertical within the dipole approximation, and only zone-center phonons are allowed by momentum conservation, so that the scattered electron remains at the same point in reciprocal space, given by the wave vector of the initial electronic state, $\mathbf{k}$, ignoring the finite wave vector of the excitation photon. Assuming that the dependence of the transition matrix elements in the numerator of Eq. (4) on the electronic transition energy $E(\mathbf{k})$ is much weaker than for the resonant denominators, we can rewrite Eq. (4) in the form of an integral over the transition energy,

$$I(E_l) = \left| M_{\text{opt}}^{\text{abs}} M_{\text{el-ph}}^{\text{S/AS}} M_{\text{opt}}^{\text{ems}} \right|^2 \times \int \left| \frac{1}{(E_l - E - i\Gamma)\,(E_l \mp \hbar\omega_{\text{ph}} - E - i\Gamma)} \right|^2 g(E)\,dE \quad (5)$$

where $g(E)$ is the JDOS profile. Strictly speaking, this assumption is not correct, since the transition matrix elements are strongly anisotropic about the K point in the Brillouin zone of the graphene layer.[42] Based on the zone-folding scheme and the approximation of the linear isotropic electronic dispersion relations around the K and K' points, the JDOS profile can be written as

$$g(E) = \text{Re} \sum_i \frac{2L}{\sqrt{3}\pi a \gamma_0} \frac{E}{\sqrt{E^2 - (E_{ii} + i\Gamma_{\text{J}})^2}} \quad (6)$$

where L is the nanotube length and i is the index of the VHS in the JDOS. i is also used here for the complex imaginary unit in front of Γ_{J}. The quantity Γ_{J} in Eq. (6) is introduced as a measure of the VHS broadening caused by finite size effects. Quantization of the electronic wave vector along the tube axis limits the maximum value of the JDOS at the VHS E_{ii} to $g(E_{ii}) = 2L^2E_{ii}/(3\pi^2a^2\gamma_0^2)$. The Γ_{J} in Eq. (6) does not affect the shape of the JDOS profile $g(E)$ for $E > E_{ii}$, introduces a weak, rapidly decaying tail for $E < E_{ii}$, and limits the maximum value of the JDOS to $g(E_{ii}) = L\sqrt{E_{ii}}/(\sqrt{3}\pi a\gamma_0\sqrt{\Gamma_{\text{J}}})$. By comparing the JDOS values at the VHS, we obtain the expression for the VHS effective width $\Gamma_{\text{J}} = 3\pi^2a^2\gamma_0^2/(4L^2E_{ii})$. For E_{ii} and Γ_{J} fitted to the experimental data,[46] we obtain the effective nanotube length $L \approx 100$ nm for the particular nanotube observed in the experiment.[46]

The resonant window defined by Eqs. (5) and (6) has a strongly asymmetric shape. Within the model used in Ref. 46 to fit the experimental data, the absolute value squared in Eq. (5) is taken not only of the resonance denominators but also of the JDOS profile $g(E)$. This results in the resonant window shown in Figure 14 by the solid line, which is less asymmetric than the resonant window given by Eqs. (5) and (6). Finally, some have suggested that the squared absolute value should be taken after integration of the resonant denominators and the JDOS profile over E in Eq. (5), or, equivalently, the squared absolute value should be taken after summation of $K(\mathbf{k})$ over $\mathbf{k}$ in Eq. (4). The latter approach allows the amplitudes of the scattered electrons to interfere. This model results in a fully symmetric resonant window with respect to the E_{ii} and $E_{ii} \pm \hbar\omega_{\text{ph}}$. Further Raman experiments taken with a tunable laser are expected to clarify the asymmetry issues related to the resonant window.

Probing VHS profiles of SWNTs by resonance Raman spectroscopy can be achieved not only by varying the laser excitation energy, as described above, but also at the fixed laser line by shifting the Fermi level electrochemically. As a first approximation, the electrochemically induced charges fill electronic states in the nanotubes following their DOS profiles, which are not affected when the electrolyte potential is changed. Charge transfer affects the force constants, which in turn results in frequency shifts of the Raman features.[48] These shifts are proportional to the amount of charge induced in the nanotube. Thus, measurements of the shifts of different Raman features vs. the electrode potential provide integrated DOS profiles for carbon nanotubes, similar to measurements of the tunneling current vs. bias voltage in STS experiments. Differentiating experimental data to obtain the DOS profile is a major source of inaccuracy for electrochemical Raman measurements of the DOS profiles as well as for STS measurements. Recently reported measurements of the G, D, and G' Raman features of SWNTs in H_2SO_4 aqueous media reveal strongly nonlinear frequency shifts vs. the electrochemical potential, reflecting the contribution of the VHSs to the DOS profiles.[49] The frequency shifts measured with two laser lines, one resonant with metallic and the other resonant

with semiconducting nanotubes in the sample, show noticeable differences arising from the absence of electronic states in the band gap of semiconducting nanotubes and their presence for metallic nanotubes.[49]

3.2. Metals and Semiconductors

SWNTs can experience either metallic (M) or semiconducting (S) behavior, depending on whether or not the cutting lines cross the degenerate K and K' points in the Brillouin zone, which in turn depends on the structural symmetry of carbon nanotubes ($n - m$ either being a multiple of 3 (metallic SWNTs) or not (semiconducting SWNTs)), as discussed in Section 2.3. This exciting property of carbon nanotubes, first predicted theoretically quite a long time ago on the basis of the zone-folding scheme,[19, 20] has by now been confirmed by many experimental techniques, such as STS,[10] transport measurements,[50] and Raman spectroscopy.[15]

SWNTs are proposed for possible use in future nanoelectronic and molecular electronic devices. This potential usage of carbon nanotubes raises the question of measuring their electronic DOS at the Fermi level, as a critical characteristic of their conducting properties. The curvature of the nanotube wall results in mini-band gaps opening up in the DOS of metallic nanotubes at the Fermi level, as discussed in Section 2.3. The mini-band gaps of zigzag metallic SWNTs of different diameters measured by STS[45] are circled by dashed lines in Figure 13. The curvature reduces the transfer integrals for carbon-carbon bonds, which in turn shifts the Fermi wave vector $\mathbf{k}_F$ (the degeneracy point in the Brillouin zone of the graphene layer) away from the K and K' points.[22, 45, 51] For zigzag SWNTs, $\mathbf{k}_F$ moves perpendicular to the cutting lines (similar to the change from M to S SWNTs shown in Fig. 7), opening mini-band gaps at the Fermi level $E_F = 0$ of M zigzag SWNTs, whereas for armchair SWNTs, $\mathbf{k}_F$ moves along the cutting line, so that armchair SWNTs remain metallic.[22, 45, 51] The widths of the mini-band gaps are on the order of the thermal energy k_BT at room temperature, so that the mini-band gaps do not affect the conducting properties of metallic nanotubes, except at very low temperatures. In contrast, the band gaps of semiconducting nanotubes are generally much larger than k_BT at room temperature, thus providing their distinct semiconducting properties.

Presumably the best way to distinguish between metallic and semiconducting nanotubes is to perform transport measurements. Because of the extremely high length-to-diameter ratio for carbon nanotubes, electrical contacts to nanotubes can be made by standard lithographic techniques. The quality of these electrical contacts is a separate issue that affects quantitative measurements of transport phenomena. The use of a semiconducting SWNT connected to two metal electrodes as a field effect transistor has been reported,[50] where the conducting behavior of the nanotube is controlled by applying a voltage to a gate electrode. The gate voltage shifts the Fermi level relative to the energy subband edges of the semiconducting nanotube between the first VHSs in the valence and conduction bands through the band gap region, thus switching the nanotube between conducting and insulating modes. When the Fermi level is set within the band gap region by the appropriate gate voltage, the bias voltage applied to the nanotube contacts can reduce the energy barriers induced by the gate voltage for charge carriers, switching the nanotube to the conducting mode. The measured source-drain current vs. bias voltage characteristics for various values of the gate voltage, taken from Ref. 50, are shown in Figure 15. These curves demonstrate highly nonlinear current vs. voltage characteristics, with the conductance varying over six orders of magnitude, as shown in the inset to Figure 15, as the gate voltage is varied at zero bias voltage. Whereas a field effect transistor made of a semiconducting nanotube has been shown to operate at room temperature,[50] a similar device made of a metallic nanotube operates only at extremely low temperatures, as previously reported,[52] since the thermal energy k_BT must be much smaller than the band gap energy, and the mini-band gaps for metallic nanotubes are much smaller than the band gaps for semiconducting nanotubes (see Section 2.3). Field effect transistors made of both semiconducting and metallic SWNTs can operate in the ballistic transport regime because of their 1D electronic structure. "Coulomb blockade" phenomena were also observed in SWNT transistors.[52] Clearly observed differences in transport properties confirm the presence of both semiconducting and metallic SWNTs, as predicted from the cutting-line approach.

Metallic or semiconducting behavior of carbon nanotubes can also be distinguished by Raman spectroscopy. One of the Raman spectral features of carbon nanotubes,

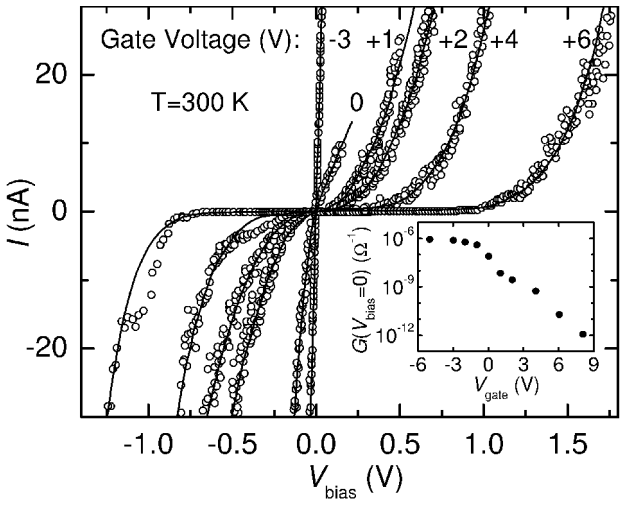

Fig. 15. Current vs. bias voltage characteristics of semiconducting nanotubes for various gate voltages at room temperature in vacuum, taken from Ref. 50. The inset shows the conductance G vs. gate voltage at zero bias voltage.

known as the *G*-band, which is formed by the tangential phonon modes, has different line shapes, depending on whether the nanotubes are metallic or semiconducting. This effect was first observed in SWNT bundles.[53] By measurement of the Raman spectra of nanotube bundles through varying the laser excitation energy, different VHSs in the JDOS of metallic and semiconducting nanotubes are probed at different E_{laser} values. Shown in Figure 16a are the *G*-band Raman features measured from nanotube bundles with a diameter distribution of 1.37 ± 0.18 nm, taken from Ref. 53, and the corresponding VHSs in the JDOS are shown in Figure 16b as a function of SWNT diameters. It is clear from Figure 16 that the *G*-band line shape, which is simply a sum of several Lorentzians for semiconducting nanotubes, changes dramatically in the case of metallic nanotubes, for which the lower components of the *G*-band Raman features have been successfully fitted by Breit-Wigner-Fano (BWF) line shapes.[41, 54] The distinction between M and S SWNTs is also found at the single-nanotube level, where the same BWF line shape appears in the *G*-band Raman feature of isolated metallic nanotubes, not aggregated in bundles.[55] Yet the intensity of the BFW line seems to be much smaller for isolated nanotubes than for SWNT bundles, with decreasing BWF intensity for increasing nanotube diameter. The intensity of the BWF line thus depends on the number of SWNTs within the bundle, which is explained by assigning the physical origin of the BWF line to a plasmon-phonon interaction in both isolated metallic SWNTs and in metallic nanotubes within SWNT bundles.[54, 56] Thus, the analysis of the *G*-band feature in the Raman spectra taken at different laser lines confirms the presence of both metallic and semiconducting nanotubes within the sample, as well as the energy locations of the cutting lines giving E^S_{ii} and E^M_{ii} VHSs in the JDOS, in agreement with the predictions of the zone-folding scheme.

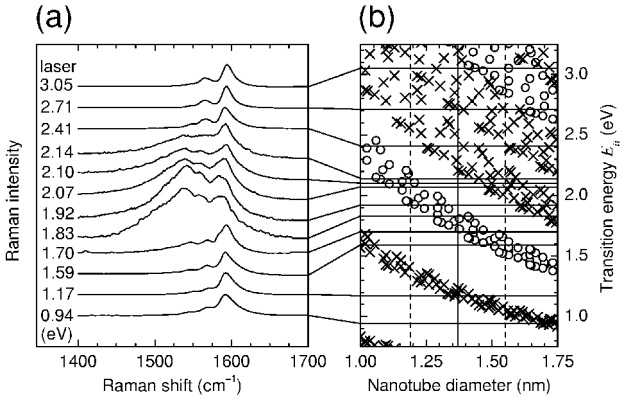

Fig. 16. (a) Raman spectra of the tangential *G*-band modes of carbon nanotube bundles measured with several different laser lines, taken from Ref. 53. (b) Resonant VHSs in the JDOS for the nanotube diameter distribution in the bundles (the vertical solid line is the average nanotube diameter and the vertical dashed lines denote the diameter distribution widths of the nanotube sample). Crosses are VHSs of semiconducting nanotubes and dots are VHSs of metallic nanotubes.

3.3. Raman Spectroscopy

Resonance Raman scattering is widely used for the characterization of SWNT bundles[6] and of isolated SWNTs.[15] Among up to 15 or 16 Raman-active zone-center phonon modes predicted by group theory[6] for chiral and achiral nanotubes, the radial-breathing mode (RBM) and the tangential *G*-band modes are the most intense features observed experimentally,[30] whereas the other modes have rather weak cross sections. In addition, some lower intensity features that are dispersive with the laser excitation energy show up in the observed Raman spectra, and the origin of these features has been explained by a second-order Raman scattering process (also commonly referred to as the double resonance mechanism).[57–59]

Six Raman-active tangential phonon modes in the frequency range of the *G*-band show different polarization dependences, in accordance with the semiclassical theory of Raman scattering. These are zone-center modes of A, E_1, and E_2 symmetries for the two in-plane optical phonon branches of the graphene layer.[6] The A symmetry modes correspond to the cutting line going through the Γ point in the 2D Brillouin zone, $\mu = 0$, the E_1 symmetry modes correspond to the two adjacent cutting lines, $\mu = \pm 1$, and the E_2 symmetry modes to the next two adjacent cutting lines, $\mu = \pm 2$, as shown in Figure 12. The basis functions for these phonon modes are summarized in the table in Figure 12. These basis functions imply that the E_2 symmetry modes appear only when both the incident and the scattered light are polarized perpendicular to the nanotube axis (so-called *XX* polarization geometry), whereas the A symmetry modes appear for both parallel (*ZZ*) and perpendicular (*XX*) polarizations of the incident/scattered light, and the E_1 symmetry modes appear only for *XZ* and *ZX* polarizations. The polarization dependence of the *G*-band has been clearly observed experimentally on an aligned bundle of SWNTs.[60]

The *G*-band profiles measured for an aligned bundle of semiconducting SWNTs in the *ZZ* and *XX* polarizations are shown in Figure 17. While both the A and E_2 symmetry

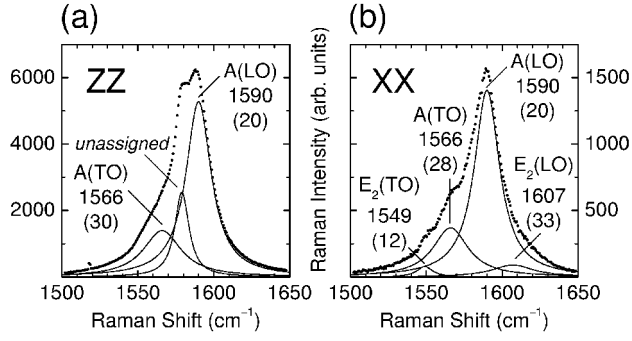

Fig. 17. Raman spectra of an aligned SWNT bundle of semiconducting SWNTs for incident/scattered light polarizations (a) parallel (*ZZ*) and (b) perpendicular (*XX*) to the SWNT bundle taken from Ref. 60 (see text for the peak assignments).

modes for the longitudinal and transverse in-plane optical phonon branches of the graphene layer (LO and TO) are observed in the *XX* polarization (see Fig. 17b), only the A symmetry modes show up in the *ZZ* polarization (see Fig. 17a), and the E_1 symmetry modes are not observed at all, in accordance with both the semiclassical theory of Raman scattering (see above) and the Raman selection rules based on the cutting lines (see Eq. (3)). The downshifts of the A symmetry TO modes from the A symmetry LO modes in Figure 17 are due to the force constant softening caused by the curvature of the nanotube wall,[55] whereas the splitting between the E_2 symmetry TO and LO modes in Figure 17b arises from both the force constant softening and the dispersion of the LO and TO phonon branches of the graphene layer at the distance $2\mathbf{K}_1$ from the Γ point in the 2D Brillouin zone. A similar polarization dependence of the *G*-band modes has recently been shown for *isolated* semiconducting SWNTs, where up to 6 phonon modes (2 A, 2 E_1, and 2 E_2) have been observed for some special polarization geometries.[43] For metallic SWNTs, the lower frequency components of the *G*-band exhibit asymmetric BWF line shapes due to plasmon-phonon coupling (see Section 3.2).

Experiments on isolated nanotubes reveal not only different polarization dependencies, but also resonances with different VHSs in the JDOS for different symmetry modes, as predicted in Section 2.6.[43] Overall, the structure of the *G*-band Raman feature appears to be much more complex in SWNTs compared with other graphitic materials, whose *G*-band appears as a single peak of E_{2g} symmetry, independent of light polarization, because the cutting lines give rise to many Raman-active modes of different symmetries (see Fig. 12). The richness in the polarization behavior of these modes reveals much information of interest to SWNTs. The results of polarization experiments for the *G*-band Raman feature in SWNTs are in good agreement with group theory predictions for the phonon modes obtained by the zone-folding scheme.

Whereas the presence of cutting lines in carbon nanotubes enriches the *G*-band in the richness of their Raman spectra compared with other graphitic materials, it also affects the dispersive Raman features,[63] arising from the double-resonance process.[57–59] Among the various double-resonance Raman features observed at the individual nanotube level, such as the defect-induced *D*-band,[64] the *M*-band and the *iTOLA* features,[65] we consider here only the most intense double-resonance Raman feature, known as the G'-band, since the G'-band dispersion is very large and therefore provides the most accurate experimental results. The G'-band appears in the Raman spectra of graphitic materials at a frequency approximately twice that of the *D*-band, and it has a two times larger dispersion (more than 100 cm^{-1}/eV) than that of the *D*-band.[66] While the *D*-band Raman feature arises from inelastic scattering of an electron by a zone-edge phonon and elastic scattering by a defect,[57–59] the G'-band is identified, in contrast, with two zone-edge phonons and appears even in highly crystalline graphitic materials which show no *D*-band intensity.

While the G'-band shows up as a single peak in most graphitic materials, it appears sometimes in the form of unusual two-peak structures at the individual nanotube level for both semiconducting[61] and metallic[62] nanotubes. The two-peak G'-band Raman features observed from semiconducting and metallic isolated nanotubes are shown in Figure 18a and b, respectively, where the (n, m) indices for these nanotubes are assigned as (15, 7) and (27, 3), following the standard procedure for identifying (n, m) indices.[67] The presence of two peaks in the G'-band Raman feature indicates the resonance of both the incident E_{laser} and scattered $E_{laser} - E_{G'}$ photons with two different VHSs of the same nanotube. The wave vectors corresponding to the resonance VHSs are shown in the unfolded 2D Brillouin zone of the graphene layer in Figure 18 below the G'-band experimental profiles. For the double-resonance process in graphite, the momentum conservation for the electron-phonon interaction couples the electronic $\mathbf{k}$ and phonon $\mathbf{q}$ wave vectors by the relation $\mathbf{q} = -2\mathbf{k}$, where both the electronic and phonon wave vectors are measured from the nearest *K* point in the Brillouin zone.[68] For the double-resonance process in carbon nanotubes, cutting lines superimposed on the 2D Brillouin zone do not change the relation $\mathbf{q} = -2\mathbf{k}$ for the 2D wave vectors.[28] Here, we consider the electronic and phonon wave vectors of the 1D nanotubes in the unfolded 2D Brillouin zone. This approach allows us to account simultaneously for both 1D wave vec-

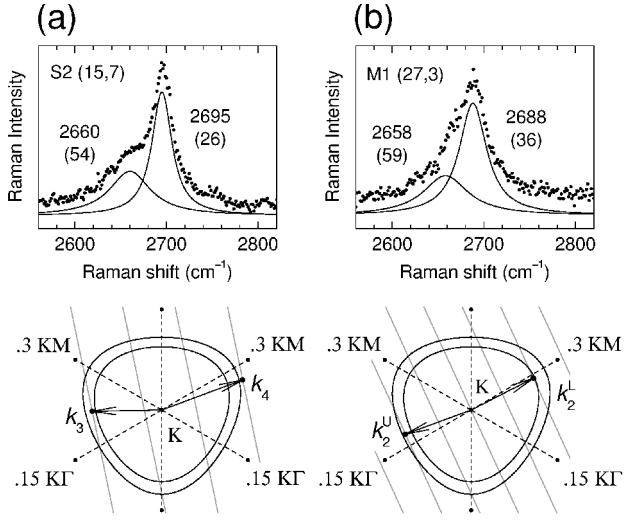

Fig. 18. The G'-band Raman features for (a) semiconducting (15, 7) and (b) metallic (27, 3) nanotubes, showing unusual two-peak structures, taken from Refs. 61 and 62, respectively. The *vicinity* of the *K* point in the unfolded Brillouin zone is shown in the lower part of the figure, where the equi-energy contours for the incident $E_{laser} = 2.41$ eV and the scattered $E_{laser} - E_{G'} = 2.08$ eV light, together with the wave vectors for the resonant VHSs ($E_{33}^S = 2.19$ eV, $E_{44}^S = 2.51$ eV, $E_{22}^{M(L)} = 2.04$ eV, $E_{22}^{M(U)} = 2.31$ eV), are also shown.

tor conservation along the nanotube axis and wave function matching in the circumferential direction.[28] The possibility of considering the electronic and phonon wave vectors of 1D nanotubes in the unfolded 2D Brillouin zone is discussed in Section 2.6.

The two peaks in Figure 18 can be associated with the phonon modes of the wave vectors $\mathbf{q}_i = -2\mathbf{k}_i$, where $i = 3$, 4, 2L, 2U and the electronic wave vectors $\mathbf{k}_i$ are shown in the lower part of Figure 18. For the semiconducting nanotube shown in Figure 18a, the resonant wave vectors $\mathbf{k}_3$ and $\mathbf{k}_4$ have different magnitudes, $k_4 - k_3 \simeq K_1/3$, resulting in twice the difference for the phonon wave vectors, $q_4 - q_3 \simeq 2K_1/3 = 4/(3d_t)$, so that the splitting of the G'-band Raman feature arises from the *phonon dispersion* $\omega_{ph}(q)$ around the K point. In contrast, for the metallic nanotube shown in Figure 18b, the resonant wave vectors $\mathbf{k}_2^L$ and $\mathbf{k}_2^U$ have roughly equal magnitudes and opposite directions away from the K point, so that the splitting of the G'-band Raman feature for metallic nanotubes arises from the *anisotropy* of the phonon dispersion $\omega_{ph}(\mathbf{q})$ around the K point.[28] Overall, the presence of two peaks in the double-resonance Raman features of isolated carbon nanotubes is associated with quantum confinement effects expressed in terms of the cutting lines. Correspondingly, the two-peak structure of the double-resonance Raman features is not observed in 2D graphitic materials. The G'-band doublet structure observed in 3D graphitic materials is attributed to the interlayer coupling.[69]

Experimentally observed two-peak structures of the double-resonance features of isolated metallic SWNTs,[62] such as the one shown in Figure 18b, is associated with anisotropy of the phonon dispersion $\omega_{ph}(\mathbf{q})$ around the K point.[28] This anisotropy can be probed by measuring double-resonance Raman features of individual SWNTs. Because of the linear electronic dispersion around the K point in the Brillouin zone of the graphene layer,[2] a given laser line selects electronic states on the circle of radius $k = E_{laser}/(\sqrt{3}\gamma_0 a)$ around the K point. The circle, however, is distorted by the electronic trigonal warping effect,[14] as shown in Figure 18. The double-resonance condition $\mathbf{q} = -2\mathbf{k}$ selects phonon wave vectors on the contour around the K point of twice the radius of the electronic contour. The cutting lines cross these equi-energy contours, as shown in Figure 18, giving rise to individual electronic states of nanotubes that are resonant with the laser line. When one of the cutting lines for a given nanotube is tangential to the equi-energy contour (see $\mathbf{k}_2^L$, $\mathbf{k}_2^U$, $\mathbf{k}_3$, and $\mathbf{k}_4$ in Fig. 18), the laser line is resonant with the corresponding VHS in the JDOS for this particular nanotube, and resonance Raman scattering can be observed from this SWNT. The position of the VHS on the equi-energy contour varies with the nanotube chiral angle θ, which determines the orientation of the cutting lines. Thus, the double-resonance process in 1D nanotubes allows us to probe individual points on the equi-energy contours in the Brillouin zone of the graphene layer. All of the points on the equi-energy contour, from $K\mathrm{M}$ to $K\Gamma$, as shown in Figure 18, can be scanned by varying the nanotube chirality from zigzag to armchair.[28] Thus, by measuring the double-resonance Raman features for SWNTs of all possible chiralities, we can reconstruct the anisotropy in the phonon dispersion $\omega_{ph}(\mathbf{q})$ around the K point.[28]

The double-resonance G'-band Raman features of many individual SWNTs of different chiralities have been measured with the laser lines 2.41 and 2.54 eV (where most of the G'-band features are fitted with a single Lorentzian and only a few show an unusual two-peak structure). For each SWNT, the (n,m) assignment is performed following the standard procedure.[67] From the (n, m) indices, the cutting lines are constructed, and the resonance VHS wave vectors $\mathbf{k}_i$ are found in the unfolded 2D Brillouin zone. The phonon wave vectors are then found from the double-resonance condition $\mathbf{q}_i = -2\mathbf{k}_i$. The frequency of the measured G'-band feature is upshifted by 35.4 $\mathrm{cm}^{-1}\mathrm{nm}/d_t$ to account for the force constant softening due to the curvature of the nanotube wall.[64] The upshifted frequency is then divided by 2 to obtain the phonon frequency, $\omega_{ph} = (\omega_{G'} - 35.4\ \mathrm{cm}^{-1}\mathrm{nm}/d_t)/2$, since there are two equivalent phonons involved in the G' scattering process. The resulting experimental points $\omega_{ph}(\mathbf{q}_i)$ are distributed all the way around the K point on the equi-energy contours corresponding to the laser excitation energies 2.41 and 2.54 eV. The force constants fitted to these experimental data $\omega_{ph}(\mathbf{q}_i)$ show anisotropy in the phonon dispersion relations around the K point.[28] At the distance $k = 0.24\ K\mathrm{M}$ from the K point (resonant with the laser line 2.41 eV), the electronic energy for the two opposite directions $K\Gamma$ and $K\mathrm{M}$ differ by 0.36 eV because of the electronic trigonal warping effect.[14] Similarly, the phonon anisotropy, or the phonon trigonal warping effect, results in a phonon frequency difference of 24 cm^{-1} for the two opposite directions $K\mathrm{M}$ and $K\Gamma$ at the distance $q = 0.24\ K\Gamma$ from the K point.[28] A measure of the electronic and phonon anisotropy is given by the ratios $\Delta E_{ii}|_{K\Gamma - K\mathrm{M}}/E_{ii} = 0.36\ \mathrm{eV}/2.49\ \mathrm{eV} = 14\%$ and $\Delta\omega_{ph}|_{K\mathrm{M}-K\Gamma}/\delta\omega_{ph} = 24\ \mathrm{cm}^{-1}/89\ \mathrm{cm}^{-1} = 27\%$, respectively, where $\delta\omega_{ph}$ is the phonon frequency change from the K point to the $q = 0.24K\Gamma$ state. These ratios show that the anisotropy, thus defined, is larger for phonons than for electrons, in part because the phonon anisotropy is probed by the double-resonance condition $\mathbf{q}_i = -2\mathbf{k}_i$ at a twice larger distance from the K point than the electronic anisotropy.

4. SUMMARY

This review of the special properties of cutting lines shows how the electronic and phonon dispersion relations of carbon nanotubes can be obtained from the electronic and phonon dispersion relations of the graphene layer following the zone-folding scheme. The singularities in the elec-

tronic density of states arising from the cutting lines are shown to affect the physical properties of carbon nanotubes dramatically. The difference from graphite properties appears most clearly in the sections of the Kataura plot (Fig. 16b) showing the most pronounced quantum confinement effects, though the two-peak structure is seen in other parts of the Kataura plot. The cutting lines can be arranged in two different ways in the reciprocal space of the graphene layer. Although the dispersion relations derived from these two different representations of the cutting lines might appear to be different at first sight, a more detailed investigation shows that the two representations are equivalent, resulting in the same physical observables. The cutting lines are shown to explain the dipole selection rules for the interaction of carbon nanotubes with photons. Selection rules for phonons are proposed based on cutting lines, and the selection rules obtained from the cutting-line analysis confirm the predictions for the Raman-active and infrared-active phonon modes made by group theory, and these selection rules explain experimental results on polarization Raman studies of carbon nanotubes.

The inaccuracy of the zone-folding scheme for the smallest-diameter nanotubes is reviewed, and this inaccuracy arises from the curvature of the tube side wall. The cutting lines defined in the reciprocal space of the flat graphene layer do not directly account for σ-π hybridization effects induced by the curvature of the graphene layer in small-diameter nanotubes, so that the zone-folding scheme requires additional corrections in the small d_t range. Experiments on recently synthesized nanotubes of diameters well below 1 nm are expected to further clarify this issue. Different experimental techniques, such as joint STM/STS studies, transport measurements, Raman spectroscopy, and optical absorption, are shown to confirm the many physical properties of carbon nanotubes that are predicted by the zone-folding scheme based on cutting lines, such as: (i) the presence of singularities in the electronic density of states, and in the joint density of states; (ii) the line shape of the van Hove singularity and its dependence on nanotube diameter and chirality; (iii) either metallic or semiconducting properties of nanotubes, depending only on their geometrical structure; and (iv) a relatively small number of Raman-active and infrared-active phonon modes, despite the large number of carbon atoms in the nanotube unit cell.

Acknowledgments: The authors gratefully acknowledge Professor Jason H. Hafner of Rice University and Professor Charles M. Lieber of Harvard University for providing the isolated single-wall carbon nanotubes on which most of the resonance Raman studies at the single-nanotube level were performed. We also thank Professor Anna K. Swan of Boston University and Professor Katrin Kneipp of the Technical University of Berlin for the many contributions they made to the research described in this review article. We are thankful to Professor C. M. Lieber and Professor Cees Dekker (of Delft University of Technology) for their kind permission to use their figures. The MIT authors acknowledge support under National Science Foundation grants DMR 01-16042 and INT 00-00408. R.S. and A.G. acknowledge a Grant-in-Aid (No. 13440091) from the Ministry of Education, Japan. A.J. and A.G.S.F., respectively, acknowledge financial support from the Brazilian agencies CNPq, under Profix (grant 350039/2002-0), and CAPES (PRODOC grant 220010182). M.A.P. acknowledges the CNPq/NSF cooperation program (CNPq grant 910120/99-4). Part of the experimental work was performed at Boston University at the Photonics Center, operated in conjunction with the Department of Physics and the department of Electrical and Computer Engineering and at the micro-Raman laboratory, Physics Department–UFMG, Brazil. This work also made use of the MRSEC Shared Facilities at MIT, supported by the National Science Foundation under grant DMR-9400334 and NSF Laser facility grant 97-08265-CHE.

References and Notes

1. M. S. Dresselhaus, G. Dresselhaus, and Ph. Avouris, *Carbon Nanotubes: Synthesis, Structure, Properties and Applications*, Vol. 80 of *Springer Series in Topics in Applied Physics*, Springer-Verlag, Berlin **(2001)**.
2. R. Saito, G. Dresselhaus, and M. S. Dresselhaus, *Physical Properties of Carbon Nanotubes*, Imperial College Press, London **(1998)**.
3. X. Blase, L. X. Benedict, E. L. Shirley, and S. G. Louie, *Phys. Rev. Lett.* 72, 1878 **(1994)**.
4. N. Wang, Z. K. Tang, G. D. Li, and J. S. Chen, *Nature* 408, 50 **(2000)**.
5. J. Sloan, A. I. Kirkland, J. L. Hutchison, and M. L. H. Green, *Chem. Commun.* 2002, 1319 **(2002)**.
6. M. S. Dresselhaus and P. C. Eklund, *Adv. Phys.* 49, 705 **(2000)**.
7. M. S. Dresselhaus, G. Dresselhaus, A. M. Rao, A. Jorio, A. G. Souza Filho, Ge. G. Samsonidze, and R. Saito, *Indian J. Phys.* 77B, 75 **(2003)**.
8. I. Cabria, J. W. Mintmire, and C. T. White, *Phys. Rev. B* 67, R121406 **(2003)**.
9. L. C. Venema, J. W. G. Wildöer, J. W. Janssen, S. J. Tans, H. L. J. Temminck Tuinstra, L. P. Kouwenhoven, and C. Dekker, *Science* 283, 52 **(1999)**.
10. J. W. G. Wildöer, L. C. Venema, A. G. Rinzler, R. E. Smalley, and C. Dekker, *Nature* 391, 59 **(1998)**.
11. M. Damnjanović, T. Vuković, and I. Milošević, *J. Phys. A: Math. Gen.* 33, 6561 **(2000)**.
12. C. T. White and J. W. Mintmire, *Nature* 394, 29 **(1998)**.
13. G. S. Painter and D. E. Ellis, *Phys. Rev. B* 1, 4747 **(1970)**.
14. R. Saito, G. Dresselhaus, and M. S. Dresselhaus, *Phys. Rev. B* 61, 2981 **(2000)**.
15. M. S. Dresselhaus, G. Dresselhaus, A. Jorio, A. G. Souza Filho, and R. Saito, *Carbon* 40, 2043 **(2002)**.
16. S. Reich, C. Thomsen, and P. Ordejón, *Phys. Rev. B* 65, 155411 **(2002)**.
17. S. Reich, J. Maultzsch, C. Thomsen, and P. Ordejón, *Phys. Rev. B* 66, 035412 **(2002)**.
18. G. Dresselhaus and M. S. Dresselhaus, in *Proceedings of the International School of Physics, Varenna on Lake Como*, edited by J. Tauc, Academic Press, San Diego, CA **(1966)**, p. 198.
19. R. Saito, M. Fujita, G. Dresselhaus, and M. S. Dresselhaus, *Appl. Phys. Lett.* 60, 2204 **(1992)**.

20. N. Hamada, S. Sawada, and A. Oshiyama, *Phys. Rev. Lett.* 68, 1579 **(1992)**.
21. C. L. Kane and E. J. Mele, *Phys. Rev. Lett.* 78, 1932 **(1997)**.
22. A. Kleiner and S. Eggert, *Phys. Rev. B* 63, 073408 **(2001)**.
23. M. Menon, E. Richter, and K. R. Subbaswamy, *J. Chem. Phys.* 104, 5875 **(1996)**.
24. O. Dubay and G. Kresse, *Phys. Rev. B* 67, 035401 **(2003)**.
25. C. Oshima, T. Aizawa, R. Souda, Y. Ishizawa, and Y. Sumiyoshi, *Solid State Commun.* 65, 1601 **(1988)**.
26. R. A. Jishi, L. Venkataraman, M. S. Dresselhaus, and G. Dresselhaus, *Chem. Phys. Lett.* 209, 77 **(1993)**.
27. A. Grüneis, R. Saito, T. Kimura, L. G. Cançado, M. A. Pimenta, A. Jorio, A. G. Souza Filho, G. Dresselhaus, and M. S. Dresselhaus, *Phys. Rev. B* 65, 155405 **(2002)**.
28. Ge. G. Samsonidze, R. Saito, A. Jorio, A. G. Souza Filho, A. Grüneis, M. A. Pimenta, G. Dresselhaus, and M. S. Dresselhaus, *Phys. Rev. Lett.* 90, 027403 **(2003)**.
29. O. E. Alon, *Phys. Rev. B* 63, R201403 **(2001)**.
30. A. M. Rao, E. Richter, S. Bandow, B. Chase, P. C. Eklund, K. W. Williams, S. Fang, K. R. Subbaswamy, M. Menon, A. Thess, R. E. Smalley, G. Dresselhaus, and M. S. Dresselhaus, *Science* 275, 187 **(1997)**.
31. J. Kürti, G. Kresse, and H. Kuzmany, *Phys. Rev. B* 58, R8869 **(1998)**.
32. D. Sanchez-Portal, E. Artacho, J. M. Solar, A. Rubio, and P. Ordejon, *Phys. Rev. B* 59, 12678 **(1999)**.
33. J. Maultzsch, S. Reich, C. Thomsen, E. Dobardzić, I. Milosević, and M. Damnjanović, *Solid State Commun.* 121, 471 **(2002)**.
34. J. Kastner, T. Pichler, H. Kuzmany, S. Curran, W. Blau, D. N. Weldon, M. Dlamesiere, S. Draper, and H. Zandbergen, *Chem. Phys. Lett.* 221, 53 **(1994)**.
35. H. Kataura, A. Kimura, Y. Ohtsuka, S. Suzuki, Y. Maniwa, T. Hanyu, and Y. Achiba, *Jpn. J. Appl. Phys. Part 2* 37, L616 **(1998)**.
36. M. J. O'Connell, S. M. Bachilo, X. B. Huffman, V. C. Moore, M. S. Strano, E. H. Haroz, K. L. Rialon, P. J. Boul, W. H. Noon, C. Kittrell, J. Ma, R. H. Hauge, R. B. Weisman, and R. E. Smalley, *Science* 297, 593 **(2002)**.
37. H. Ajiki and T. Ando, *Physica B* 201, 349 **(1994)**.
38. G. S. Duesberg, I. Loa, M. Burghard, K. Syassen, and S. Roth, *Phys. Rev. Lett.* 85, 5436 **(2000)**.
39. A. Jorio, A. G. Souza Filho, V. W. Brar, A. K. Swan, M. S. Ünlü, B. B. Goldberg, A. Righi, J. H. Hafner, C. M. Lieber, R. Saito, G. Dresselhaus, and M. S. Dresselhaus, *Phys. Rev. B* 65, R121402 **(2002)**.
40. I. Božović, N. Božović, and M. Damnjanović, *Phys. Rev. B* 62, 6971 **(2000)**.
41. H. Kataura, Y. Kumazawa, Y. Maniwa, I. Umezu, S. Suzuki, Y. Ohtsuka, and Y. Achiba, *Synth. Met.* 103, 2555 **(1999)**.
42. A. Grüneis, R. Saito, Ge. G. Samsonidze, T. Kimura, M. A. Pimenta, A. Jorio, A. G. Souza Filho, G. Dresselhaus, and M. S. Dresselhaus, *Phys. Rev. B* 67, 165402 **(2003)**.
43. A. Jorio, M. A. Pimenta, A. G. Souza Filho, Ge. G. Samsonidze, A. K. Swan, M. S. Ünlü, B. B. Goldberg, R. Saito, G. Dresselhaus, and M. S. Dresselhaus, *Phys. Rev. Lett.* 90, 107403 **(2003)**.
44. R. Saito, A. Jorio, J. H. Hafner, C. M. Lieber, M. Hunter, T. McClure, G. Dresselhaus, and M. S. Dresselhaus, *Phys. Rev. B* 64, 085312 **(2001)**.
45. M. Ouyang, J. L. Huan, C. L. Cheung, and C. M. Lieber, *Science* 292, 702 **(2001)**.
46. A. Jorio, A. G. Souza Filho, G. Dresselhaus, M. S. Dresselhaus, R. Saito, J. H. Hafner, C. M. Lieber, F. M. Matinaga, M. S. S. Dantas, and M. A. Pimenta, *Phys. Rev. B* 63, 245416 **(2001)**.
47. R. M. Martin and L. M. Falicov, in *Light Scattering in Solids, Springer Series in Topics in Applied Physics,* edited by M. Cardona, Springer-Verlag, Berlin **(1983)**, Vol. 8, p. 70.
48. G. U. Sumanasekera, J. L. Allen, S. Fang, A. L. Loper, A. M. Rao, and P. C. Eklund, *J. Phys. Chem.* 103, 4292 **(1999)**.
49. P. Corio, P. S. Santos, V. W. Brar, Ge. G. Samsonidze, S. G. Chou, and M. S. Dresselhaus, *Chem. Phys. Lett.* 370, 675 **(2003)**.
50. S. J. Tans, R. M. Verschueren, and C. Dekker, *Nature* 393, 49 **(1998)**.
51. R. Saito, M. Fujita, G. Dresselhaus, and M. S. Dresselhaus, *Phys. Rev. B* 46, 1804 **(1992)**.
52. S. J. Tans, M. H. Devoret, H. Dai, A. Thess, R. E. Smalley, L. J. Geerligs, and C. Dekker, *Nature* 386, 474 **(1997)**.
53. M. A. Pimenta, A. Marucci, S. Empedocles, M. Bawendi, E. B. Hanlon, A. M. Rao, P. C. Eklund, R. E. Smalley, G. Dresselhaus, and M. S. Dresselhaus, *Phys. Rev. B* 58, R16016 **(1998)**.
54. S. D. M. Brown, A. Jorio, P. Corio, M. S. Dresselhaus, G. Dresselhaus, R. Saito, and K. Kneipp, *Phys. Rev. B* 63, 155414 **(2001)**.
55. A. Jorio, A. G. Souza Filho, G. Dresselhaus, M. S. Dresselhaus, A. K. Swan, M. S. Ünlü, B. Goldberg, M. A. Pimenta, J. H. Hafner, C. M. Lieber, and R. Saito, *Phys. Rev. B* 65, 155412 **(2002)**.
56. C. Jiang, K. Kempa, J. Zhao, U. Schlecht, U. Kolb, T. Basché, M. Burghard, and A. Mews, *Phys. Rev. B* 66, 161404 **(2002)**.
57. A. V. Baranov, A. N. Bekhterev, Y. S. Bobovich, and V. I. Petrov, *Opt. Spectrosk.* 62, 1036 **(1987)** [*Opt. Spectrosc.* 62, 612 **(1987)**].
58. C. Thomsen and S. Reich, *Phys. Rev. Lett.* 85, 5214 **(2000)**.
59. R. Saito, A. Jorio, A. G. Souza Filho, G. Dresselhaus, M. S. Dresselhaus, and M. A. Pimenta, *Phys. Rev. Lett.* 88, 027401 **(2002)**.
60. A. Jorio, G. Dresselhaus, M. S. Dresselhaus, M. Souza, M. S. S. Dantas, M. A. Pimenta, A. M. Rao, R. Saito, C. Liu, and H. M. Cheng, *Phys. Rev. Lett.* 85, 2617 **(2000)**.
61. A. G. Souza Filho, A. Jorio, Anna K. Swan, M. S. Ünlü, B. B. Goldberg, R. Saito, J. H. Hafner, C. M. Lieber, M. A. Pimenta, G. Dresselhaus, and M. S. Dresselhaus, *Phys. Rev. B* 65, 085417 **(2002)**.
62. A. G. Souza Filho, A. Jorio, Ge. G. Samsonidze, G. Dresselhaus, M. S. Dresselhaus, A. K. Swan, M. S. Ünlü, B. B. Goldberg, R. Saito, J. H. Hafner, C. M. Lieber, and M. A. Pimenta, *Chem. Phys. Lett.* 354, 62 **(2002)**.
63. A. G. Souza Filho, A. Jorio, G. Dresselhaus, M. S. Dresselhaus, R. Saito, A. K. Swan, M. S. Ünlü, B. B. Goldberg, J. H. Hafner, C. M. Lieber, and M. A. Pimenta, *Phys. Rev. B* 65, 035404 **(2002)**.
64. A. G. Souza Filho, A. Jorio, Ge. G. Samsonidze, G. Dresselhaus, M. A. Pimenta, M. S. Dresselhaus, A. K. Swan, M. S. Ünlü, B. B. Goldberg, and R. Saito, *Phys. Rev. B* 67, 035427 **(2003)**.
65. V. W. Brar, Ge. G. Samsonidze, G. Dresselhaus, M. S. Dresselhaus, R. Saito, A. K. Swan, M. S. Ünlü, B. B. Goldberg, A. G. Souza Filho, and A. Jorio, *Phys. Rev. B* 66, 155418 **(2002)**.
66. M. A. Pimenta, E. B. Hanlon, A. Marucci, P. Corio, S. D. M. Brown, S. A. Empedocles, M. G. Bawendi, G. Dresselhaus, and M. S. Dresselhaus, *Brazilian J. Phys.* 30, 423 **(2000)**.
67. A. Jorio, R. Saito, J. H. Hafner, C. M. Lieber, M. Hunter, T. McClure, G. Dresselhaus, and M. S. Dresselhaus, *Phys. Rev. Lett.* 86, 1118 **(2001)**.
68. R. Saito, A. Jorio, A. G. Souza Filho, G. Dresselhaus, M. S. Dresselhaus, A. Grüneis, L. G. Cançado, and M. A. Pimenta, *Jpn. J. Appl. Phys.* 41, 4878 **(2002)**.
69. H. Wilhelm, M. Lelausian, E. McRae, and B. Humbert, *J. Appl. Phys.* 84, 6552 **(1998)**.

Received: 1 May 2003. Revised/Accepted: 4 June 2003.